Master Thesis

Multi Phase Field Modeling for Fiber Reinforced Composites

carried out for the purpose of obtaining the degree of
Diplom-Ingenieur_in (Dipl.-Ing. or DI),

submitted at TU Wien
Faculty of Mechanical and Industrial Engineering
by
Rafael Fleischhacker
Mat.No.: 11813840

under supervision of

Associate Prof. Dipl.-Ing. Dr.techn. Heinz Pettermann
Univ.Ass. Pavan Kumar Asur Vijaya Kumar, PhD

Institute of Lightweight Design and Structural Biomechanics

Vienna, 19th March 2025

I confirm, that the printing of this thesis requires the approval of the examination board.

Affidavit

I declare in lieu of oath, that I wrote this thesis and carried out the associated research myself, using only the literature cited in this volume. If text passages from sources are used literally, they are marked as such.

I confirm that this work is original and has not been submitted for examination elsewhere, nor is it currently under consideration for a thesis elsewhere. I acknowledge that the submitted work will be checked electronically-technically using suitable and state-of-the-art means (plagiarism detection software). On the one hand, this ensures that the submitted work was prepared according to the high-quality standards within the applicable rules to ensure good scientific practice "Code of Conduct" at the TU Wien. On the other hand, a comparison with other student theses avoids violations of my personal copyright.

Vienna, 19th March 2025

Acknowledgements

Firstly, I want to thank my thesis adviser Heinz E. Pettermann for his continuous help and guidance. If I felt like I did not know how to proceed, an hour of discussion helped me understand what to do next. I always knew what to do or try next when leaving your office.

Secondly, I want to thank Pavan Kumar Asur Vijaya Kumar for continuously lending me an ear when I needed one. Our discussions, regardless of if they concerned the topic of the present thesis or not, were always intellectually stimulating and fun.

Additionally, I sincerely acknowledge that I am allowed to use the pictures of compact tension tests done by Professor Zoltan Major and Andreas Kapshammer from the Institute of Polymer Product Engineering, Johannes Kepler University, Linz, Austria to compare them to the numerical results.

I want to thank my friends for always managing to get my mind off of work and my parents for their never-ending support.

Last but not least, I want to thank my partner Anke, who always listened to the ramblings about my thesis even though she did not understand most of it.

Contents

Abstract

This thesis aims to propose a two-dimensional multi-phase field method for modeling damage in fiber reinforced composite materials. Two damage (phase field) variables are introduced each representing damage in fiber and matrix, respectively. Damage is initiated by Puck's failure criteria, while the propogation is ensured by the phase field methods driven by the energy in the fiber and matrix respectively. The proposed model is implemented as a finite element user-code in the commercial package Abaqus. The efficiency of the model is subsequently tested in a single ply setting by showing seven different test cases with different fiber directions in each case. The crack patterns and force displacement behaviors are shown and results are compared to experimental work. Specifically, the qualitative comparison of the crack patterns with different fiber orientations showed an excellent match to various experimental results. Quantitatively, an open-hole tension test with two different fiber directions provided a good match to experimental data. Since fiber reinforced composites are almost always used as laminates with different fiber directions, the current implementation is also tested for cross ply laminates using the mesh overlay method. This method provides a simple way to represent laminated composites in a two-dimensional setting. In spite of the restrictions stemming from the two dimensional method, the proposed model shows excellent results in comparison with experiments. Specifically, three cases are tested as follows: Firstly, tensile and compressive failure of unnotched specimens is tested, the quantitative results are compared to numerical results. Secondly, open-hole tension results with two different layup sequences are used to qualitatively and quantitatively compare with the experimental results. Lastly, the compact tension test of a cross-ply laminate is presented to showcase the capability of the proposed model. The results are shown to correlate very well with the experimental results in spite of not modeling delamination.

Kurzfassung

Die vorliegende Arbeit zeigt ein zweidimensionales Multi-Phase Field Modell zur Schadensmodellierung von faserverstärkten Kunststoffen. Hierfür werden zwei Schadensvariablen eingeführt, die die Schädigung von Faser- und Matrixmaterial getrennt repräsentieren. Puck's Festigkeitskriterium wird dabei als Kriterium für den Start der Schädigung eingesetzt. Nachdem besagtes Kriterium erfüllt ist, wird die Schädigung von der Phase Field Methode fortgesetzt. Das Modell ist als Finite Elemente Benutzercode im kommerziellen Programm Abaqus implementiert. Validiert wird das Modell anhand von sieben Testfällen, die einlagige faserverstärkte Kunststoffe behandeln. Um den Einfluss der Faserrichtung auf die Schadensformen zu untersuchen, beinhaltet jeder Testfall mehrere Faserorientierungen. Qualitativ stimmen die simulierten Rissmuster exzellent mit den Mustern, die in Experimenten beobachtet wurden. Zusätzlich wird das Kraft-Verformungs Verhalten einer Lochplatte unter Zugbelastung mit experimentellen Ergebnissen verglichen. Auch hier zeigt das Modell gute Übereinstimmung mit den experimentellen Beobachtungen. Da faserverstärkte Kunststoffe meistens als Laminat mit mehreren Schichten unterschiedlicher Faserorientierung verwendet werden, wird die Mesh Overlay Methode verwendet, um verschiedene Faserorientierungen in einem zweidimensionalen Modell repräsentieren zu können. Trotz der Limitierungen, die mit dieser Methode einhergehen, zeigt das Modell exzellente Übereinstimmung mit experimentellen Ergebnissen. Als Vergleich werden drei Testfälle herangezogen. Der Vergleich mit numerischen Ergebnissen für Zug- und Druckversuche von ungekerbten Proben mit drei verschiedenen Laminataufbauten zeigt gute Übereinstimmung. Des weiteren wird der Zugversuch von Lochplatten mit zwei verschiedenen Laminataufbauten behandelt. Die entstehenden Rissmuster zeigen sehr gute Übereinstimmung mit numerischen Ergebnissen, während die maximal auftretenden Kräfte gute Korrelation mit experimentellen Beobachtungen zeigen. Schließlich wird das Kraft-Verformungs Verhalten eines Kompakt-Zugversuchs mit dem entsprechenden Experiment verglichen. Sowohl die entstehenden Rissmuster als auch das Kraft-Verformungs Verhalten zeigt sehr gute Übereinstimmung. Die auftretenden Kräfte werden vom vorliegenden Modell dabei überschätzt, was aber auf die fehlende Modellierung von Delamination zurückgeführt werden kann.

List of Figures

List of Tables

1 Introduction

1.1 Motivation

Saving weight in various engineering applications is paramount for mechanical systems to remain energy efficient. An ideal mechanical component would weigh nothing while still withstanding all forces present in the system without yielding or damage. Therefore, high strength to weight ratios are highly sought for in order to remain as energy efficient as possible. That is where fiber-reinforced composite materials come into play. Due to their high strength to weight ratios, they are increasingly important in various industrial applications. While they are most commonly used in aerospace applications, they are also utilized in wind turbines, sporting equipment, the automobile industry, as well as in the public transportation sector. In all these applications, they are used as structural components as part of sandwich structures, where fiber-reinforced composites provide high stiffness as thin face layers. Since fiber-reinforced composites give structural strength and the core is relatively weak compared to the composite, the composite is the critical component in such structures. If the composite fails in a sandwich structure, the whole structure fails. Therefore, it is important to understand the different failure mechanism that occur in fiber-reinforced composites.

Although fiber-reinforced composites are already widely used, the fracture behavior of these materials is still the subject of intensive research, due to their inherent anisotropic material behavior. Composite material are generally composed of two or more distinct materials with clearly identifiable interfaces between them. In fiber-reinforced composites, there are only two materials present, namely the matrix and the fiber. Due to their inherently anisotropic behavior, fiber-reinforced composite materials show failure modes that are more complicated than those of other more standard materials. Failures related to matrix and fiber breaking individually are named intralaminar failure. Similarly, the failure of the bonding between matrix and fiber also falls in this category. Since in this thesis, only long fiber-reinforced composites are considered, the material is strong in fiber direction and weak in the direction transverse to the fiber. This can be mitigated to a certain extent by creating a lay up of differently oriented fiber-reinforced composite plies. Consequently, leading to strong structures in multiple directions. Furthermore, this introduces even more complexity into the failure of these materials as the bonding between the individual plies can now fail too, leading to delamination. In addition, intralaminar matrix cracks can appear in individual plies, while the other plies are still intact, weakening the structure as a whole without directly leading to catastrophic failures. Consequently, this thesis propose a robust failure prediction theory using the well known phase field method based on [1] to predict fracture in fiber-reinforced composites.

1.2 Numerical Models for Failure in fiber-reinforced Composites

The different failure modes mentioned in the previous section sparked a wide range of experimental research. For example, emerging crack patterns [2, 3] are investigated or the delamination behavior is studied [2, 4, 5]. There has been a wide range of attempts to simulate the fracture in fiber-reinforced composites using finite element methods in general. For example, cohesive zone models were used to predict delamination events in composite materials [6–8]. Cohesive zone models work with a special type of finite element that needs to be placed where the crack will form. Consequently, the crack path must be known in advance, resulting in a lack of predictive capabilities if the crack path is not known. Furthermore, a structure that contains cohesive elements in its entire mesh suffers from computational expense. Continuum damage mechanics models generally do not rely on a predetermined crack path and are therefore more suitable for such failure modes [9–17]. In general, these models incorporate damage variables that are activated by damage activation functions, which allows the prediction of crack nucleation. Therefore simulations of crack patterns are possible without prior knowledge of the emerging crack patterns.

On the other hand, the phase-field method has been introduced by Francfort and Marigo [18] and presents a novel approach for crack propagation. These methods were first implemented by Bourdin et al. [19]. The phase-field method is based on Griffith's theory of brittle fracture [20] and modifies said theory in such a way that the discontinuous nature of the sharp crack is approximated using a smoothed surface. In short, the phase-field method approximates the energy it takes to create new surfaces using a diffusive damage variable, referred to as Phase-field. Furthermore, additional criteria such as Puck failure modes can be incorporated in phase field approach to predict fracture initiation, while the fracture propagation is done using phase-field approach. Furthermore, due to the continuous boundaries, phase field methods can predict crack paths without prior knowledge of the fracture behavior. Until now the phase-field method has been successfully used in various applications, such as predicting brittle failure in isotropic materials [21] as well as being applied to ductile failures [22] and fatigue [23]. Furthermore, the phase-field method has been implemented for functionally graded materials [24] to name a few.

Different approaches for modelling fiber-reinforced composites have been studied in the phase field literature. Specifically, Reinoso et al. [25] have developed a phase-field model for fiber-reinforced composites with only one damage variable, Bleyer and Alessi [26] have implemented a similar model but with two damage variables leading to a multi-phase-field formulation. A multi-phase-field formulation has the advantage of splitting the accumulated damage into its fiber and matrix contributions. The inherent advantage of the phase-field method in this scenario is its ability to predict crack patterns in materials without any special ad hoc criterion. Not only intralaminar failures can be captured but also delamination and delamination migration, as shown in [27, 28]. The latter used a combination of cohesive-like elements and the phase-field method, combining the advantages of each of the models. In addition, there is the possibility to adopt phenomenological failure theories into the formulation, leading to more efficient methods where crack nucleation and propagation can be achieved in a single model. Phenomenological theories such as Puck's failure theory [29] have been successfully implemented by Dean et al. [1] leading to the present thesis that aims to improve the phase-field formulation presented therein regarding its crack prediction capabilities. Matrix dominated failures generally form along the fiber direction as shown in [3]. Virtually all previous implementations of the phase-field model in the context of fiber-reinforced composites were not able to accurately predict this behavior [27, 30–33]. The present thesis aims to alleviate this problem and verify a phase-field model showing more accurate crack patterns than previous works while still maintaining a good quantitative match to experimental work.

The remaining thesis is structured as follows. Section 2 aims to provide a general overview of the general phase-field model with a subsequent specialization to fiber-reinforced composite materials. This section also provides a short explanation of Puck's failure theory as well as the implementation of the model as a user-defined subroutine in the commercial finite element software Abaqus/Standard 2022 (Dassault Systèmes Simulia Corp., Providence, RI, USA). Section 3 shows the application of the formulation to single ply composite materials while section 4 provides results about laminated composite materials using the mesh overlay technique. Section 4 also gives a brief explanation of mesh overlay technique and its implications. Afterwards, sections 5 and 6 provide a conclusion that summarizes the results of this thesis and an outlook on what the current model can be expected to bring in the future.

2 Methodology

This section aims to give a short overview of the general phase-field method and subsequently focusing on its adaptation to fiber-reinforced composite materials. Furthermore, Puck's failure theory, is explained in the sequel which is used to initiate the damage, followed by a brief discussion on the driving forces.

2.1 General Phase-Field Formulation

2.1.1 Variational Formulation

Griffith's theory [20] states that the macroscopic occurrence of cracks is the result of microscopic debonding at the crystalline level. In other words, the microscopic debonding needs the energy equivalent it takes to move two atoms apart creating a new surface. Francfort and Marigo [18] took this idea and formulated a variational formulation suitable for brittle fracture resulting in an energy minimization problem.

With n_{dim} representing an Euclidean dimension, consider an arbitrary body $\mathcal{B} \in \mathbb{R}^{n_{dim}}$ with its delimiting boundaries denoted as $\partial\mathcal{B} \in \mathbb{R}^{n_{dim}-1}$ and the crack set denoted as $\Gamma \in \mathbb{R}^{n_{dim}-1}$. Define a vector valued kinematic displacement field $\mathbf{u}(\mathbf{x},t) : \mathcal{B} \times [0,t] \to \mathbb{R}^{n_{dim}}$, with $\tau \in [0,t]$ being pseudo time. Furthermore, $\mathbf{x} \in \mathcal{B}$ denotes the position vector. The displacement field $\mathbf{u}(\mathbf{x},t)$ induces strains in the body, which is represented by the strain tensor $\boldsymbol{\varepsilon} : \mathcal{B} \to \mathbb{R}^{n_{dim} \times n_{dim}}$ is calculated by taking the symmetric gradient of the displacement field $\mathbf{u}(\mathbf{x},t)$, which leads to

$$\boldsymbol{\varepsilon}(\mathbf{u}) = \left(\frac{\nabla\mathbf{u} + \nabla\mathbf{u}^T}{2}\right). \tag{1}$$

The displacement field $\mathbf{u}(\mathbf{x},t)$ is a consequence of the applied displacement boundary conditions $\bar{\mathbf{u}}$ and traction boundary conditions $\mathbf{t} = \sigma \cdot \mathbf{n}$ acting on the boundaries $\partial\mathcal{B}_\mathbf{u}$ and $\partial\mathcal{B}_\mathbf{t}$, respectively. Here σ denotes the Cauchy stress tensor and $\mathbf{n}$ is an outwards facing unit normal vector. The boundaries $\partial\mathcal{B}_\mathbf{u}$ and $\partial\mathcal{B}_\mathbf{t}$ fulfill both $\overline{\partial\mathcal{B}_\mathbf{u} \cup \partial\mathcal{B}_\mathbf{t}} = \partial\mathcal{B}$ and $\partial\mathcal{B}_\mathbf{u} \cap \partial\mathcal{B}_\mathbf{t} = \emptyset$. Lastly, body force densities $\mathbf{f}_v : \mathcal{B} \to \mathbb{R}^{n_{dim}}$ can act on the body $\mathcal{B}$.

With this at hand, the total energy Π of the body $\mathcal{B}$ is composed of the strain energy Π_s, the applied external energy Π_{ext} and the fracture or surface energy $\mathcal{W}$. The total energy takes the form

$$\Pi(\mathbf{u}, \Gamma) = \Pi_s(\mathbf{u}) - \Pi_{ext}(\mathbf{u}) + \mathcal{W}(\Gamma). \tag{2}$$

The applied external energy can be split into its body force and traction contributions as

$$\Pi_{\mathrm{ext}}(\mathbf{u}) = \int_{\mathcal{B}} \mathbf{f}_v \cdot \mathbf{u} \, \mathrm{dx} + \int_{\partial\mathcal{B}_t} \mathbf{t} \cdot \mathbf{u} \, \mathrm{dS}. \tag{3}$$

By defining a strain energy density Ψ, the strain energy can also be written in an integral form as follows

$$\Pi_{\mathrm{s}}(\mathbf{u}) = \int_{\mathcal{B}\setminus\Gamma} \Psi(\boldsymbol{\varepsilon}) \, \mathrm{dx}. \tag{4}$$

The fracture energy can be represented using the fracture energy density G_{c} as

$$\mathcal{W}(\Gamma) = \int_{\Gamma} G_{\mathrm{c}} \, \mathrm{dS}, \tag{5}$$

completing the formulation shown in equation (2). The total energy now takes the form

$$\Pi(\mathbf{u},\Gamma) = \int_{\mathcal{B}\setminus\Gamma} \Psi(\boldsymbol{\varepsilon}) \, \mathrm{dx} - \int_{\mathcal{B}} \mathbf{f}_v \cdot \mathbf{u} \, \mathrm{dx} - \int_{\partial\mathcal{B}_t} \mathbf{t} \cdot \mathbf{u} \, \mathrm{dS} + \int_{\Gamma} G_{\mathrm{c}} \, \mathrm{dS}. \tag{6}$$

The solution to the above equation (6), can be found as a minimization of the energy with respect to the displacement field $\mathbf{u}_t$ and the unknown crack set Γ_t within a discrete time step t as follows

$$(\mathbf{u}_t, \Gamma_t) = \operatorname*{argmin}_{S} \; \Pi(\mathbf{u},\Gamma). \tag{7}$$

Here, S is a condition such that the crack surface Γ can only grow monotonically. In other words, it ensures only solutions that fulfill $\dot{\Gamma} \geq 0$ are found. If $\dot{\Gamma} < 0$, cracks would be able to heal, violating the second law of thermodynamics. Furthermore, this minimization problem is hard to solve due to the discontinuous sharp crack set Γ .

2.1.2 Phase-Field Method

As stated previously, the discontinuities sharp cracks introduced by fracture are very hard to deal with. Therefore, phase-field is introduced to alleviate this problem as it smears out the sharp crack path yielding a smooth transition from fully intact to fully damaged material. This is achieved by introducing a scalar field called as phase-field such that $\mathfrak{d} \in [0,1]$ signifying that the material is fully intact, if $\mathfrak{d} = 0$, while fully damaged material leads to $\mathfrak{d} = 1$. Additionally, a characteristic length scale $\ell \in \mathbb{R}^+$ has to be introduced to scale the width of the damage variable. Modifying equation (5) as in [34] yields

$$\mathcal{W}(\Gamma) = \int_{\Gamma} G_{\mathrm{c}} \, \mathrm{dS} \approx \int_{\mathcal{B}} \frac{G_{\mathrm{c}}}{4c_w} \left(\frac{\alpha(\mathfrak{d})}{\ell} + \ell \mid \nabla\mathfrak{d} \mid^2 \right) \mathrm{dx}. \tag{8}$$

Here, $\alpha(\mathfrak{d})$ is the geometric crack function, which establishes how the phase-field variable $\mathfrak{d}$ distributes over the domain. Naturally, it satisfies $\alpha(0) = 0$ and $\alpha(1) = 1$. This function can be arbitrarily chosen, as long as the above conditions are fulfilled. An assortment of typical functions can be found in section 2.1.3. In order to normalize the geometric crack function, $c_w := \int_0^1 \sqrt{\alpha(s)}\, ds$ is introduced. Since the phase-field method regularizes the crack set Γ, the strain energy has to be altered. Due to the competition of strain and fracture energy, the strain energy is made to deteriorate if a crack grows. Therefore, an energetic crack degradation function $g(\mathfrak{d})$ mapping [0,1] to [1,0] has to be introduced. The regularized strain energy then takes the following form

$$\Pi_{\mathrm{s}}(\mathbf{u}, \Gamma) = \int_{\mathcal{B}\setminus\Gamma} \Psi(\boldsymbol{\varepsilon})\, \mathrm{dx} \approx \int_{\mathcal{B}} g(\mathfrak{d})\Psi_0(\boldsymbol{\varepsilon})\, \mathrm{dx}. \tag{9}$$

Here Ψ_0 is the initial strain energy density of intact material. With these regularized energies, one can now rewrite the total energy functional from equation (6) as

$$\Pi(\mathbf{u},\mathfrak{d}) = \int_{\mathcal{B}} g(\mathfrak{d})\Psi_0(\boldsymbol{\varepsilon})\, \mathrm{dx} + \int_{\mathcal{B}} \frac{G_{\mathrm{c}}}{4c_w}\left(\frac{\alpha(\mathfrak{d})}{\ell} + \ell \mid \nabla\mathfrak{d} \mid^2\right) \mathrm{dx} - \Pi_{ext}(\mathbf{u}). \tag{10}$$

Now, one has to determine $(\mathbf{u}^*, \mathfrak{d}^*)$ from the minimization problem in equation (7). That is

$$(\mathbf{u}^*, \mathfrak{d}^*) = \underset{S_{\mathfrak{d}}}{\operatorname{argmin}}\ \Pi(\mathbf{u},\mathfrak{d}), \tag{11}$$

with $S_{\mathfrak{d}} = \{\dot{\mathfrak{d}} \geq 0 \text{ for all } \mathbf{x} \in \mathcal{B}\}$ being the condition that the damage variable $\mathfrak{d}$ can only grow, so as to follow the second law of thermodynamics.
The remaining unknowns for this problems, besides $(\mathbf{u}, \mathfrak{d})$, are the degradation function $g(\mathfrak{d})$ and the geometric crack function $\alpha(\mathfrak{d})$. Both of these can be arbitrarily chosen as long as they fulfill the conditions stated before. However, there are certain recommended functions that have been suggested by previous research. They are briefly shown in the next section.

2.1.3 Choice of degradation and geometric crack functions

Apart from the conditions $\alpha(0) = 0$ and $\alpha(1) = 1$, there are no restrictions imposed on the geometric crack function. Therefore, previous research suggests a number of different functions for $\alpha(\mathfrak{d})$, which consequently also determine the normalization factor c_w. Similarly, the energetic degradation function $g(\mathfrak{d})$ has to be chosen, with the conditions being $g(0) = 1$ signifying the fully intact state, and $g(1) = 0$ corresponding to a fully damaged state. Additionally, $g(\mathfrak{d})$ has to be a

$\alpha(\mathfrak{d})$	$g(\mathfrak{d})$	c_w	Citing Articles
$\mathfrak{d}$	$(1-\mathfrak{d})^2$	$2/3$	[35], [19] (AT-1)
$\mathfrak{d}^2$	$(1-\mathfrak{d})^2$	$1/2$	[19] (AT-2)
$2\mathfrak{d}-\mathfrak{d}^2$	$\frac{(1-\mathfrak{d})^p}{(1-\mathfrak{d})^p+Q(\mathfrak{d})}$, $Q(\mathfrak{d}) = a_1\mathfrak{d} + a_1a_2\mathfrak{d}^2 + a_1a_2a_3\mathfrak{d}^3$	$\pi/4$	[36] (PFCZM)

Table 1: Common geometric crack functions in the literature.

monotonically decreasing function and $\frac{dg}{d\mathfrak{d}} < 0$. The different suggested models and the corresponding research are listed in table 1.

The three most important models are shown in table 1 with the AT1 and AT2-models being the most common models. The model chosen for this thesis is the AT2-model owing to ease of implementation, and computational efficiency. Additionally, the boundedness of the damage variable $\mathfrak{d} \in [0,1]$ can be enforced by selecting a corresponding driving force.

2.2 Multi Phase-Field formulation

2.2.1 Variational formulation

In order to model fiber-reinforced composites in a phase field framework considering that damage in fiber and matrix separately[1], crack set Γ is divided into a crack set corresponding to fiber failure Γ_f and a crack set corresponding to matrix failure Γ_m, such that $\Gamma_f, \Gamma_m \subset \mathbb{R}^{n-1}$, and $\Gamma_f \cup \Gamma_m = \Gamma$. The current implementation is based on the model used in [1], hence it utilizes two phase-field variables each representing damage in fiber and matrix $\mathfrak{d}_f$ and $\mathfrak{d}_m$ to approximate the crack sets, respectively. Each phase field variable possesses one characteristic length scale, which are denoted as ℓ_f and ℓ_m in the following. Therefore, the general energy functional in equation (10) has to be modified to accommodate the newly introduced damage variables. For this purpose the individual energies have to be split up into their fiber and matrix components. Furthermore, based on [1] , the total internal energy of the system in fiber-reinforced composites can be composed of

1. The strain energy Π_f stemming from fiber.
2. The strain energy Π_m stemming from the matrix.
3. The applied external energy Π_{ext}.
4. The fracture energy $\mathcal{W}_f$ corresponding to fiber failure, and

---

[1] Fiber dominated failure and matrix dominated failure modes are called fiber and matrix damage or failure for the sake of brevity.

5. the fracture energy $\mathcal{W}_m$ corresponding to matrix failure.

Similarly to equation (2), the total internal energy for a fiber-reinforced composite takes the form

$$\Pi(\mathbf{u}, \Gamma_f, \Gamma_m) = \Pi_f(\mathbf{u}) + \Pi_m(\mathbf{u}) + \mathcal{W}_f(\Gamma_f) + \mathcal{W}_m(\Gamma_m) - \Pi_{ext}(\mathbf{u}). \tag{12}$$

As mentioned before, fracture is seen as a competition between strain energy and the energy it takes to create new surfaces. The latter is the aforementioned fracture energy. In the present multi-phase field model, the strain energy of the fiber creates a pair of new surfaces corresponding to fiber failure. Comparably, a pair of new surfaces corresponding to matrix failure is created by the strain energy of the matrix. Taking into account Griffith's theory, leads to the total energy functional being

$$\begin{aligned}\Pi(\mathbf{u},\Gamma_f,\Gamma_m) = \int_{\mathcal{B}\setminus\Gamma_f} \Psi_f(\boldsymbol{\varepsilon})\ \mathrm{dx} + \int_{\mathcal{B}\setminus\Gamma_m} \Psi_m(\boldsymbol{\varepsilon})\ \mathrm{dx} - \Pi_{ext} \\ + \int_{\Gamma_f} G_{\mathrm{c,f}}\ \mathrm{dS} + \int_{\Gamma_m} G_{\mathrm{c,m}}\ \mathrm{dS}.\end{aligned} \tag{13}$$

Here, $G_{\mathrm{c,f}}$ and $G_{\mathrm{c,m}}$ are the fracture energy densities corresponding to fiber and matrix failure, respectively. Similarly, $\Psi_f(\boldsymbol{\varepsilon})$ and $\Psi_m(\boldsymbol{\varepsilon})$ denote the undamaged strain energy densities for fiber and matrix, respectively. Lastly, the external work $\Pi_{ext}(\mathbf{u})$ can be formulated the same way as in equation (3). The crack sets corresponding to fiber and matrix failure Γ_f and Γ_m are unknown in the equation (13) and are approximated by the two phase fields $\mathfrak{d}_f$ and $\mathfrak{d}_m$. This is represented as

$$\begin{aligned}\mathcal{W}_i(\Gamma_i) = \int_{\Gamma_i} G_{\mathrm{c},i}\ \mathrm{dS} \approx \int_{\mathcal{B}} \frac{G_{\mathrm{c},i}}{4c_w} \left(\frac{\alpha(\mathfrak{d}_i)}{\ell_i} + \ell_i \left[\nabla\mathfrak{d}_{\mathrm{i}} \cdot \mathcal{A}_i \cdot \nabla\mathfrak{d}_i \right] \right)\ \mathrm{dx}, \\ \text{with } i = f,\ m.\end{aligned} \tag{14}$$

As mentioned before, the AT2 model is chosen, which leads to the geometric crack function being represented by $\alpha(\mathfrak{d}_i) = \mathfrak{d}_i^2$ $(i = f{,}m)$. Lastly, the non-local part in equation (14) is penalized by the structural tensors $\mathcal{A}_f$ and $\mathcal{A}_m$. They are defined by the principle material directions e_1 corresponding to the fiber direction and e_2 corresponding to the transverse in-plane direction. This is written as

$$\mathcal{A}_f = e_2 \otimes e_2, \quad \text{and} \quad \mathcal{A}_m = e_1 \otimes e_1. \tag{15}$$

For the fiber orientation θ measured from the global x-coordinate, the material basis functions e_1, and e_2 are written as

$$e_1 = \begin{bmatrix} \cos\theta \\ \sin\theta \end{bmatrix}, \quad \text{and} \quad e_2 = \begin{bmatrix} \sin\theta \\ \cos\theta \end{bmatrix}. \tag{16}$$

In short, the structural tensors $\mathcal{A}_f$, and $\mathcal{A}_m$ alter the non-local part of the fracture energy in a way that penalizes the corresponding material directions. Notice that the weak form which is required for the determination of the elemental stiffness and the residual of the variational problem, is computed in a global coordinate system. Since Puck's failure theory is based on the stress state $\boldsymbol{\sigma}$ in principle material direction, a global and local coordinate system have to be introduced in the following. To differentiate between quantities in the local and global orientation, the notations $(\cdot)^{\mathcal{L}}$ and $(\cdot)^{\mathcal{G}}$ are introduced to denote the local and global coordinate system, respectively. For the purpose of formulating a consistent two-dimensional model, a plane stress state is assumed due to the plies being small in thickness compared to their span-wise dimensions. Additionally, the Voigt notation is adopted to represent the constitutive tensor structure. The resulting stress and strain vectors takes the form

$$\boldsymbol{\sigma} = \begin{bmatrix} \sigma_{11} \\ \sigma_{22} \\ \sigma_{12} \end{bmatrix}, \quad \text{and} \quad \boldsymbol{\varepsilon} = \begin{bmatrix} \varepsilon_{11} \\ \varepsilon_{22} \\ \gamma_{12} \end{bmatrix}. \tag{17}$$

Therein, γ_{12} denotes the shear angle. With this in mind, the corresponding constitutive elasticity matrix $\mathbb{C}$ can be introduced. In order to represent each quantity in the local or global coordinate system, the transformation matrix $\mathcal{R}$ is introduced according to [37]. It is given as

$$\mathcal{R} = \begin{bmatrix} (\cos\theta)^2 & (\sin\theta)^2 & 2\sin\theta\cos\theta \\ (\sin\theta)^2 & (\cos\theta)^2 & -2\sin\theta\cos\theta \\ -\cos\theta\sin\theta & \cos\theta\sin\theta & (\cos\theta)^2-(\sin\theta)^2 \end{bmatrix}. \tag{18}$$

The relation of the strain field in the local and global setting then becomes

$$\boldsymbol{\varepsilon}^{\mathcal{L}} = \mathcal{R}^{-T} \cdot \boldsymbol{\varepsilon}^{\mathcal{G}}. \tag{19}$$

The constitutive elasticity matrix $\mathbb{C}^{\mathcal{L}}$ which relates the stress state to the strain state in the local setting can be transformed to the global setting as

$$\mathbb{C}^{\mathcal{G}} = \mathcal{R}^{-1} \cdot \mathbb{C}^{\mathcal{L}} \cdot \mathcal{R}^{-T} \tag{20}$$

With this matrix, the stress in the global coordinate system is computed as

$$\boldsymbol{\sigma}^{\mathcal{G}} = \mathbb{C}^{\mathcal{G}} \cdot \boldsymbol{\varepsilon}^{\mathcal{G}}. \tag{21}$$

Consequently, the stress state in the local orientation can be determined with the transformation matrix $\mathcal{R}$ as

$$\boldsymbol{\sigma}^{\mathcal{L}} = \mathcal{R} \cdot \boldsymbol{\sigma}^{\mathcal{G}}. \tag{22}$$

The constitutive elasticity matrix corresponding to the fiber in the local setting $\mathbb{C}_f^{\mathcal{L}}$ can be written as

$$\mathbb{C}_f^{\mathcal{L}} = \begin{bmatrix} C_{11} & 0 & 0 \\ 0 & 0 & 0 \\ 0 & 0 & 0 \end{bmatrix}, \tag{23}$$

with $C_{11} = \frac{E_{11}}{1-\nu_{12}\nu_{21}}$. Here, E_{11} denotes the longitudinal Young's modulus of the ply while ν_{12} is the minor and $\nu_{21} = \nu_{12}\frac{E_{11}}{E_{22}}$ the major Poisson's ratio of the ply. Additionally, E_{22} represents the transverse Young's modulus of the ply. With this at hand, the strain energy density linked to the fiber becomes

$$\Psi_f(\mathbf{u},\mathfrak{d}_f) = \mathbf{g}(\mathfrak{d})\frac{1}{2}\,(\boldsymbol{\varepsilon}^{\mathcal{L}})^T : \mathbb{C}_f^{\mathcal{L}} : \boldsymbol{\varepsilon}^{\mathcal{L}}. \tag{24}$$

Here, $\mathbf{g}(\mathfrak{d})$ denotes the combination of the degradation functions for matrix and fiber material and is presented in detail in the sequel. A similar formulation can be derived for the matrix contribution to the strain energy. Here, the constitutive elasticity matrix corresponding to the material in the local setting $\mathbb{C}_m^{\mathcal{L}}$ is written as

$$\mathbb{C}_m^{\mathcal{L}} = \begin{bmatrix} 0 & C_{12} & 0 \\ C_{12} & C_{22} & 0 \\ 0 & 0 & C_{33} \end{bmatrix}. \tag{25}$$

Here, $C_{33} = G_{12}$ denotes the shear modulus of the ply. Furthermore, the rest of the components in equation (25) are $C_{12} = \frac{\nu_{12}E_{11}}{1-\nu_{12}\nu_{21}}$ and $C_{22} = \frac{E_{22}}{1-\nu_{12}\nu_{21}}$. Consequently, the matrix contribution to the strain energy density becomes

$$\Psi_m(\mathbf{u},\mathfrak{d}) = \mathbf{g}(\mathfrak{d})\frac{1}{2}\,(\boldsymbol{\varepsilon}^{\mathcal{L}})^T : \mathbb{C}_m^{\mathcal{L}} : \boldsymbol{\varepsilon}^{\mathcal{L}}. \tag{26}$$

The total energy of the system in equation (13) can now be written as

$$\begin{aligned} \Pi(\mathbf{u},\, \mathfrak{d}_f,\, \mathfrak{d}_m) = {} & \int_{\mathcal{B}} \mathbf{g}(\mathfrak{d})\; \frac{1}{2}\; (\boldsymbol{\varepsilon}^{\mathcal{L}})^T : \mathbb{C}_f^{\mathcal{L}} : \boldsymbol{\varepsilon}^{\mathcal{L}} \;\mathrm{dx} + \int_{\mathcal{B}} \mathbf{g}(\mathfrak{d})\; \frac{1}{2}\; (\boldsymbol{\varepsilon}^{\mathcal{L}})^T : \mathbb{C}_m^{\mathcal{L}} : \boldsymbol{\varepsilon}^{\mathcal{L}} \;\mathrm{dx} \\ & -\Pi_{ext}(\mathbf{u}) + \int_{\mathcal{B}} \frac{G_{c,f}}{4c_w}\left(\frac{\alpha(\mathfrak{d}_f)}{\ell_f} + \ell_f\left[\nabla\mathfrak{d}_f \cdot \mathcal{A}_f \cdot \nabla\mathfrak{d}_f\right]\right)\;\mathrm{dx} \\ & + \int_{\mathcal{B}} \frac{G_{c,m}}{4c_w}\left(\frac{\alpha(\mathfrak{d}_m)}{\ell_m} + \ell_m\left[\nabla\mathfrak{d}_m \cdot \mathcal{A}_m \cdot \nabla\mathfrak{d}_m\right]\right)\;\mathrm{dx}. \end{aligned} \tag{27}$$

Because of the additive decomposition of the strain energy into the fiber and matrix contributions and the fact that all the strain energies are in local material orientation, the total internal energy can be written in a compact form as follows

$$
\begin{aligned}
\Pi(\mathbf{u}, \mathfrak{d}_f, \mathfrak{d}_m) = & \int_{\mathcal{B}} \mathbf{g}(\mathfrak{d}) \, \frac{1}{2} \, (\boldsymbol{\varepsilon}^{\mathcal{L}})^T : \mathbb{C}^{\mathcal{L}} : \boldsymbol{\varepsilon}^{\mathcal{L}} \, \mathrm{dx} - \Pi_{ext}(\mathbf{u}) \\
& + \int_{\mathcal{B}} \frac{G_{\mathrm{c},f}}{4c_w} \left(\frac{\alpha(\mathfrak{d}_f)}{\ell_f} + \ell_f \left[\nabla \mathfrak{d}_f \cdot \mathcal{A}_f \cdot \nabla \mathfrak{d}_f \right] \right) \, \mathrm{dx} \\
& + \int_{\mathcal{B}} \frac{G_{\mathrm{c},m}}{4c_w} \left(\frac{\alpha(\mathfrak{d}_m)}{\ell_m} + \ell_m \left[\nabla \mathfrak{d}_m \cdot \mathcal{A}_m \cdot \nabla \mathfrak{d}_m \right] \right) \, \mathrm{dx}.
\end{aligned}
\tag{28}
$$

The total anisotropic constitutive stiffness matrix $\mathbb{C}^{\mathcal{L}}$ therein reads

$$
\mathbb{C}^{\mathcal{L}} = \mathbb{C}_f^{\mathcal{L}} + \mathbb{C}_m^{\mathcal{L}}, \tag{29}
$$

which leads to

$$
\mathbb{C}^{\mathcal{L}} = \begin{bmatrix} C_{11} & C_{12} & 0 \\ C_{12} & C_{22} & 0 \\ 0 & 0 & G_{12} \end{bmatrix}. \tag{30}
$$

Furthermore, a constitutive stiffness matrix of the damaged material $\tilde{\mathbb{C}}^{\mathcal{L}}$ can be introduced, whose specific form reads

$$
\tilde{\mathbb{C}}^{\mathcal{L}} = \mathbf{g}(\mathfrak{d}) \mathbb{C}_f^{\mathcal{L}} + \mathbf{g}(\mathfrak{d}) \mathbb{C}_m^{\mathcal{L}}, \tag{31}
$$

$$
\begin{aligned}
\tilde{\mathbb{C}}^{\mathcal{L}} = & \begin{bmatrix} g_f \\ g_m \\ \min(g_f, g_m) \end{bmatrix}^T \cdot \begin{bmatrix} C_{11} & C_{12} & 0 \\ C_{12} & C_{22} & 0 \\ 0 & 0 & G_{12} \end{bmatrix} = \\
& \begin{bmatrix} g_f C_{11} & g_m C_{12} & 0 \\ g_m C_{12} & g_m C_{22} & 0 \\ 0 & 0 & \min(g_f, g_m) G_{12} \end{bmatrix}.
\end{aligned}
\tag{32}
$$

In line with the AT2 degradation functions, $g_f = (1 - \mathfrak{d}_f)^2$ and $g_m = (1 - \mathfrak{d}_m)^2$ is chosen. With these degradation functions, the degraded stresses due to damage can be formulated in the local and global reference systems as follows

$$
\tilde{\boldsymbol{\sigma}}^{\mathcal{L}} = \mathbf{g}(\mathfrak{d})^T \cdot \boldsymbol{\sigma}^{\mathcal{L}}, \quad \tilde{\boldsymbol{\sigma}}^{\mathcal{G}} = \mathcal{R}^{-1} \cdot \tilde{\boldsymbol{\sigma}}^{\mathcal{L}}. \tag{33}
$$

The degraded stresses are needed in both the local and the global setting due to Puck's failure theory, which is evaluated in the local orientation. With the total energy at hand, the functional can be solved for $(\mathbf{u},\, \mathfrak{d}_f,\, \mathfrak{d}_m)$ at every discrete time step $\tau \in [0{,}t]$ from the minimization problem

$$(\mathbf{u}^*{,}\mathfrak{d}_f^*{,}\mathfrak{d}_m^*) = \underset{\mathcal{S}}{\operatorname{argmin}}\; \Pi(\mathbf{u},\, \mathfrak{d}_f,\, \mathfrak{d}_m), \tag{34}$$

with $\mathcal{S} = \{\dot{\mathfrak{d}}_f{,}\dot{\mathfrak{d}}_m \geq 0 \text{ for all } \mathbf{x} \in \mathcal{B}\}$ being the condition that the damage variables $\mathfrak{d}_f$ and $\mathfrak{d}_m$ can only grow.

2.2.2 Puck's Failure Theory

In order to accurately model the initiation of damage, a failure criterion is needed. For this purpose, Puck's failure theory [29] is used as a failure criterion since it distinguishes between fiber and matrix dominated failure. This leads to damage being initiated by Puck's failure criterion while the damage progression is handled by the driving forces behind the phase-field approach.

Puck's theory is based entirely on the local coordinate, consequently, the 1-direction denotes the fiber direction, while the 2-direction represents the in-plane transverse direction to the fiber direction. Puck's failure theory distinguishes five modes of failure, two corresponding to fiber failure and three corresponding to matrix failure. The two fiber failure modes are fiber tension and compression. For matrix dominated failure, Puck failure theory can distinguish three different Modes, namely Mode A, Mode B and Mode C. Mode A handles the case of transverse tension which leads to matrix cracks along the fiber direction. Mode B and C both handle transverse compression by incorporating a fracture plane characterized by a fracture angle θ_{fp}. A visualization of the action plane concept for these modes can be seen in figure 1. While this angle is zero for Mode B it is non-zero for Mode C. All of these modes are distinguished by energetic considerations depending on the loading state of the problem. If the corresponding exposure factor reaches a value of one, failure is initiated. Despite the model being two-dimensional, the action plane can be evaluated if Mode C is triggered, but it can not be shown in the results in this case. For Mode A and Mode B the fracture angle becomes $\theta_{fp} = 0°$.

In addition to the already introduced material parameters, Puck's failure theory considers the tensile strengths in the fiber direction R_{11}^T, in the direction transverse to the fiber direction R_{22}^T, and the shear strength R_{12} of the ply. For the purpose of handling compressive loads, the compressive strengths in the fiber direction R_{11}^C and the direction transverse to the fiber direction R_{22}^C are required as well. Lastly, the matrix inclination parameters P_{21}^+, P_{21}^-, P_{22}^+ and P_{22}^- are mostly dependent on the type of fiber that is used within the composite.

Regarding fiber failure, the exposure factors F_f^T and F_f^C trigger fiber failure in tension and compression, respectively, if they reach a value of one. For tensile

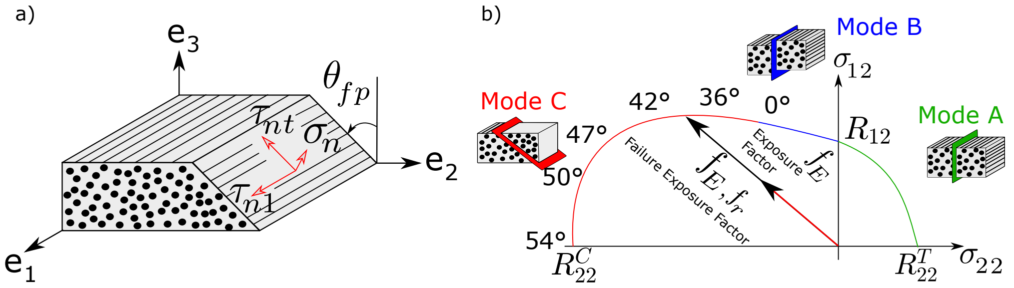

Figure 1: a) Action plane concept of Puck's failure theory [29] including the definitions of active stresses on the fracture plane inclined by the angle θ_{fp} and b) visualization of the exposure factor f_E and the exposure factor at failure $f_{E,fr}$. The image is taken from [1] and modified for better readability including changes to match the following notations.

fiber failure, the exposure factor F_f^T is simply the ratio of the stresses in the fiber direction $\sigma_{11}^{\mathcal{L}}$ to the tensile strength of the ply in the fiber direction R_{11}^T i.e

$$F_f^T = \frac{\sigma_{11}^{\mathcal{L}}}{R_{11}^T}, \quad \text{if} \quad \sigma_{11}^{\mathcal{L}} \geq 0. \tag{35}$$

The exposure factor for fiber failure in compression is also dependent on the shear stresses acting on the material, leading to the formulation

$$F_f^C = \sqrt{\left(\frac{\sigma_{11}^{\mathcal{L}}}{R_{11}^C}\right)^2 + \alpha \left(\frac{\sigma_{12}^{\mathcal{L}}}{R_{12}}\right)^2}, \quad \text{if} \quad \sigma_{11}^{\mathcal{L}} < 0. \tag{36}$$

Therein, $\alpha \in [0,1]$ is a parameter for characterizing the influence of shear stresses in compressive fiber failure.
For transverse tension matrix failure or Mode A failure, the exposure factor F_m^T takes both the tensile and the shear stresses in the material into account, leading to

$$F_m^T = \sqrt{\left(\frac{\sigma_{12}^{\mathcal{L}}}{R_{12}}\right)^2 + \left(1 - P_{21}^+ \frac{\sigma_{22}^{\mathcal{L}}}{R_{12}}\right)^2 + \left(\frac{\sigma_{22}^{\mathcal{L}}}{R_{22}^T}\right)^2} + \frac{P_{21}^+ \sigma_{22}^{\mathcal{L}}}{R_{12}}, \quad \text{if} \quad \sigma_{22}^{\mathcal{L}} > 0. \tag{37}$$

Regarding Mode B failure, the exposure factor assumes the form

$$F_m^C = \sqrt{\left(\frac{\sigma_{12}^{\mathcal{L}}}{R_{12}}\right)^2 + \left(P_{21}^- \frac{\sigma_{22}^{\mathcal{L}}}{R_{12}}\right)^2} + \frac{P_{21}^- \sigma_{22}^{\mathcal{L}}}{R_{12}}, \text{if } \sigma_{22}^{\mathcal{L}} < 0 \text{ and } \left[\left| \frac{\sigma_{22}^{\mathcal{L}}}{\sigma_{12}^{\mathcal{L}}} \right| < \left| \frac{R_{22}^a}{R_{12}^C} \right| \right], \tag{38}$$

where $R_{22}^{a} = \frac{R_{12}}{2P_{21}^{-}}\left(\sqrt{1+2P_{21}^{-}\frac{R_{22}^{C}}{R_{12}}}-1\right)$, and $R_{12}^{C} = R_{12}\sqrt{1+2P_{22}^{-}}$.

Lastly, Mode C failure is triggered if $\sigma_{22}^{\mathcal{L}} < 0$ and $\left[\left|\frac{\sigma_{12}^{\mathcal{L}}}{\sigma_{22}^{\mathcal{L}}}\right| < \left|\frac{R_{12}^{C}}{R_{22}^{a}}\right|\right]$ which leads to the exposure factor becoming

$$F_m^C = \left(\frac{\sigma_{12}^{\mathcal{L}}}{2(1+P_{22}^{-})R_{12}}\right)^2 - \left(\frac{\sigma_{22}^{\mathcal{L}}}{R_{22}^{C}}\right)^2 \frac{R_{22}^{C}}{\sigma_{22}^{\mathcal{L}}}. \tag{39}$$

2.2.3 Implementation in Finite Element Setting

The previously established theory is implemented in a finite element setting as a user subroutine UEL in the commercial software Abaqus in this section based on the implementation in [1]. The minimization problem in equation (34) can be solved for the variables $(\mathbf{u},\ \mathfrak{d}_f,\ \mathfrak{d}_m)$, by taking first variation of equation (28). Consequently, weak forms with the test functions $(\delta\mathbf{u},\ \delta\mathfrak{d}_f,\ \delta\mathfrak{d}_m)$ take the form

$$\int_{\mathcal{B}} \tilde{\boldsymbol{\sigma}}^{\mathcal{G}} : \boldsymbol{\varepsilon}^{\mathcal{G}}(\delta\mathbf{u})\mathrm{dx} - \int_{\mathcal{B}} \boldsymbol{f_v}\cdot\delta\mathbf{u}\,\mathrm{dx} + \int_{\partial\mathcal{B}_t} \bar{\mathbf{t}}\cdot\delta\mathbf{u}\,dS = 0, \tag{40}$$

$$\int_{\mathcal{B}} G_{C,f}\left(\frac{\mathfrak{d}_f}{\ell_f}\delta\mathfrak{d}_f + \ell_f\nabla\mathfrak{d}_f\mathcal{A}_f\nabla\delta\mathfrak{d}_f\right)\mathrm{dx} - \int_{\mathcal{B}}\left(\tilde{\boldsymbol{\sigma}}^{\mathcal{G}} : \boldsymbol{\varepsilon}^{\mathcal{G}}\delta\mathfrak{d}_f\right)\mathrm{dx} = 0, \tag{41}$$

$$\int_{\mathcal{B}} G_{C,m}\left(\frac{\mathfrak{d}_m}{\ell_m}\delta\mathfrak{d}_m + \ell_m\nabla\mathfrak{d}_m\mathcal{A}_m\nabla\delta\mathfrak{d}_m\right)\mathrm{dx} - \int_{\mathcal{B}}\left(\tilde{\boldsymbol{\sigma}}^{\mathcal{G}} : \boldsymbol{\varepsilon}^{\mathcal{G}}\delta\mathfrak{d}_m\right)\mathrm{dx} = 0. \tag{42}$$

The domain $\mathcal{B}$ is now split into n_e isoparametric elements. Using the standard Bubnov-Galerkin methods, the interpolation functions for $(\mathbf{u},\ \mathfrak{d}_f,\ \mathfrak{d}_m)$ can be written as

$$\mathbf{u}^e = \sum_{i=1}^{n_e}\mathbf{N}_i^u\mathbf{u}_i^e, \quad \mathfrak{d}_f^e = \sum_{i=1}^{n_e}N_i^{\mathfrak{d}}\mathfrak{d}_{f,i}^e, \quad \mathfrak{d}_m^e = \sum_{i=1}^{n_e}N_i^{\mathfrak{d}}\mathfrak{d}_{m,i}^e, \tag{43}$$

where $\mathbf{N}_i^u$ and $N_i^{\mathfrak{d}}$ are the shape functions for the displacement field and the damage variables, respectively. The derivatives of the shape functions are called $\mathbf{B}_i^u$ and $B_i^{\mathfrak{d}}$, which leads to the derivatives of the interpolated fields becoming

$$\nabla\mathbf{u}^e = \sum_{i=1}^{n_e}\mathbf{B}_i^u\mathbf{u}_i^e, \quad \nabla\mathfrak{d}_f^e = \sum_{i=1}^{n_e}B_i^{\mathfrak{d}}\mathfrak{d}_{f,i}^e, \quad \nabla\mathfrak{d}_m^e = \sum_{i=1}^{n_e}B_i^{\mathfrak{d}}\mathfrak{d}_{m,i}^e. \tag{44}$$

With this and the fact that the variational test functions $(\delta\mathbf{u},\ \delta\mathfrak{d}_f,\ \delta\mathfrak{d}_m)$ are interpolated using the same shape functions as $(\mathbf{u},\ \mathfrak{d}_f,\ \mathfrak{d}_m)$, a discrete version of the elemental residual vectors can be written down. These residual vectors are then written as

$$\mathbf{R}^e_{\mathbf{u}} = \int_{\mathcal{B}} (\mathbf{B}^u)^T \tilde{\sigma}^{\mathcal{G}} d\mathbf{x} - \int_{\mathcal{B}} (\mathbf{N}^u)^T \mathbf{f}_v d\mathbf{x} - \int_{\partial\mathcal{B}} (\mathbf{N}^u)^T \overline{\mathbf{t}}\; dS, \tag{45}$$

$$\mathbf{R}^e_f = \int_{\mathcal{B}} -2(1-\mathfrak{d}_f)(\mathbf{N}^{\mathfrak{d}})^T \mathcal{H}_f + \frac{G_{C,f}}{\ell_f}\left((\mathbf{N}^{\mathfrak{d}})^T \mathfrak{d}_f + \ell_f^2 (\mathbf{B}^{\mathfrak{d}})^T \mathcal{A}_f \nabla \mathfrak{d}_f\right) d\mathbf{x}, \tag{46}$$

$$\mathbf{R}^e_m = \int_{\mathcal{B}} -2(1-\mathfrak{d}_m)(\mathbf{N}^{\mathfrak{d}})^T \mathcal{H}_m + \frac{G_{C,m}}{\ell_m}\left((\mathbf{N}^{\mathfrak{d}})^T \mathfrak{d}_m + \ell_m^2 (\mathbf{B}^{\mathfrak{d}})^T \mathcal{A}_m \nabla \mathfrak{d}_m\right) d\mathbf{x}. \tag{47}$$

Here, $\mathcal{H}_i$, $i = f{,}m$ are the phase-field driving forces which ensure the irreversibility of the phase-field variables as

$$\mathcal{H}_i = \max_{\tau\in[0,T]} \left\{ \zeta_i \left(\frac{\Psi_i}{\Psi_{i,0}} - 1 \right) \right\} \quad \text{if} \;\; \Psi_{i,0} > 0, \text{ and } 0 \text{ otherwise}, \quad i = f{,}m. \tag{48}$$

The factors ζ_i, $i = f{,}m$ are dimensionless parameters to scale the driving forces. This can be seen as a parameter that can be calibrated based on the experiment. The terms $\Psi_{i,0}$, $i = f{,}m$ are the strain energy densities corresponding to fiber and matrix at which Puck initiation occurs. It can be expressed as

$$\Psi_{f,0} = \begin{cases} \dfrac{1}{2}\sigma^{\mathcal{L}}_{11}\varepsilon^{\mathcal{L}}_{11} & \text{if } F^T_f{,}F^C_f = 1 \\ 0 & \text{if } F^T_f{,}F^C_f < 1 \end{cases} \tag{49}$$

$$\Psi_{m,0} = \begin{cases} \dfrac{1}{2}\left(\sigma^{\mathcal{L}}_{22}\varepsilon^{\mathcal{L}}_{22} + 2\sigma^{\mathcal{L}}_{12}\varepsilon^{\mathcal{L}}_{12}\right) & \text{if } F^T_m{,}F^C_m = 1 \\ 0 & \text{if } F^T_m{,}F^C_m < 1 \end{cases} \tag{50}$$

The residual vectors of fiber failure and matrix failure are decoupled as seen in equations (46) and (47). On the other hand, both of these residuals are coupled to the equilibrium condition in equation (45). As Abaqus already comes with a built-in robust Newton-Raphson solver with automatic time stepping,the residual equations can be shown as a Newton-Raphson iteration at time step $(n+1)$ as

$$\begin{bmatrix} \mathbf{u} \\ \mathfrak{d}_f \\ \mathfrak{d}_m \end{bmatrix}_{n+1} = \begin{bmatrix} \mathbf{u} \\ \mathfrak{d}_f \\ \mathfrak{d}_m \end{bmatrix}_{n} - \begin{bmatrix} K^{\mathbf{uu}} & 0 & 0 \\ 0 & K^{ff} & 0 \\ 0 & 0 & K^{mm} \end{bmatrix}^{-1}_{n+1} \begin{bmatrix} \mathbf{R}_{\mathbf{u}} \\ \mathbf{R}_f \\ \mathbf{R}_m \end{bmatrix}_{n}. \tag{51}$$

Therein, the elemental stiffness matrix consists of the derivatives of the elemental residual vectors with regards to their respective variables $(\mathbf{u},\, \mathfrak{d}_f,\, \mathfrak{d}_m)$. The specific terms can be written as

$$K^{\mathbf{uu}} := \frac{\partial \mathbf{R}^e_{\mathbf{u}}}{\partial \mathbf{u}^e} = \int_{\mathcal{B}} (\mathbf{B}^u)^T \, \tilde{\mathbb{C}}^{\mathcal{G}} \mathbf{B}^u \, d\mathbf{x}, \tag{52}$$

$$K^{ff} := \frac{\partial \mathbf{R}^e_f}{\partial \mathfrak{d}^e_f} = \int_{\mathcal{B}} \left(2\mathcal{H}_f + \frac{G_{c,f}}{\ell_f} \right) (\mathbf{N}^{\mathfrak{d}})^T \mathbf{N}^{\mathfrak{d}} + G_{c,f}\ell_f (\mathbf{B}^{\mathfrak{d}})^T \mathcal{A}_f \mathbf{B}^{\mathfrak{d}} \, d\mathbf{x}, \tag{53}$$

$$K^{mm} := \frac{\partial \mathbf{R}^e_m}{\partial \mathfrak{d}^e_m} = \int_{\mathcal{B}} \left(2\mathcal{H}_m + \frac{G_{c,m}}{\ell_m} \right) (\mathbf{N}^{\mathfrak{d}})^T \mathbf{N}^{\mathfrak{d}} + G_{c,m}\ell_m (\mathbf{B}^{\mathfrak{d}})^T \mathcal{A}_m \mathbf{B}^{\mathfrak{d}} \, d\mathbf{x} \tag{54}$$

The system of equations in equation (51) can now be implemented in a UEL subroutine compatible with Abaqus. The general algorithm works as follows with $(\delta \mathbf{u}^n,\ \delta \mathfrak{d}^n_f,\ \delta \mathfrak{d}^n_m)$ given as an input at increment n to calculate an output $(\delta \mathbf{u}^{n+1},\ \delta \mathfrak{d}^{n+1}_f,\ \delta \mathfrak{d}^{n+1}_m)$ for increment $(n+1)$:

1. Evaluate rotation tensor $\mathcal{R}$.
2. Evaluate structural tensors $\mathcal{A}_f$ and $\mathcal{A}_m$
3. Start the loop over all integration points based on the previous time increment t_n.
   (a) Evaluate shape functions $\mathbf{N}^u_i$, $N^{\mathfrak{d}}_i$ and their derivatives $\mathbf{B}^u_i$, $B^{\mathfrak{d}}_i$.
   (b) Interpolate the phase-field variables $\mathfrak{d}_f$, $\mathfrak{d}_m$ to the integration points.
   (c) Evaluate strains in both the global and local coordinate systems $\boldsymbol{\varepsilon}^{\mathcal{G}} = \mathbf{B}^u_i \mathbf{u}^n$, $\boldsymbol{\varepsilon}^{\mathcal{L}} = \mathcal{R}^{-T} \boldsymbol{\varepsilon}^{\mathcal{G}}$.
   (d) Build constitutive elasticity matrix in the local setting $\mathbb{C}^{\mathcal{L}}$ and compute the equivalent in the global setting through $\mathbb{C}^{\mathcal{G}} = \mathcal{R}^{-1} \mathbb{C}^{\mathcal{L}} \mathcal{R}^{-T}$.
   (e) Evaluate the stresses in the global coordinate system $\boldsymbol{\sigma}^{\mathcal{G}} = \mathbb{C}^{\mathcal{G}} \boldsymbol{\varepsilon}^{\mathcal{G}}$ and subsequently rotate them into the local system by $\boldsymbol{\sigma}^{\mathcal{L}} = \mathcal{R} \boldsymbol{\sigma}^{\mathcal{G}}$.
   (f) Calculate the corresponding Puck exposure factors with the stresses in the local setting $\boldsymbol{\sigma}^{\mathcal{L}}$.
   (g) Calculate the strain energy for fiber Ψ_f and matrix Ψ_m individually in order to evaluate the driving forces $\mathcal{H}_f$ and $\mathcal{H}_m$.
   (h) Evaluate the degraded constitutive stiffness matrix in the local coordinate system $\tilde{\mathbb{C}}^{\mathcal{L}}$.
   (i) Compute the degraded stresses in the local $\tilde{\boldsymbol{\sigma}}^{\mathcal{L}}$ and global coordinate systems $\tilde{\boldsymbol{\sigma}}^{\mathcal{G}}$
   (j) Evaluate the residual vectors in equations (45), (46) and (47) as well as the stiffness matrix in equation (51).
4. Assemble the final element matrices as well as the internal force vectors and perform the final assembly.

E_{11} (MPa)	E_{22} (MPa)	ν_{12}	ν_{21}	G_{12} (MPa)
114800	11700	0.0222	0.21	9600

Table 2: Elastic Properties of the composites.

R_{11}^T (MPa)	R_{22}^T (MPa)	R_{11}^C (MPa)	R_{22}^C (MPa)	R_{12} (MPa)
2000	70	1650	240	105

Table 3: Strength properties of the composites.

3 Numerical Examples for Single Ply Composites

This section concerns the performance of the current model in terms of its predictive capabilities of the fracture behavior of single plies. For this purpose, seven different numerical examples are carried out with them being (i) single-edge notched tension, (ii) open hole tension, (iii) compact tension, (iv) centre notched tension, (v) three-point bending, (vi) bi-material interface, and (vii) unnotched tension specimens with artificial defects. While the first four examples are qualitatively and quantitatively compared to experimental results [3, 38], cases (v), (vi), and (vii) are supposed to show the further capabilities of the proposed model. Each of the examples is done with the same set of fiber orientation θ that ranges from $-60°$ to $90°$ in order to show the potential of the model regarding the prediction of the orientation of the emerging crack patterns. The material parameters for the examples are shown in tables 2 to 5 and apply to all examples unless stated otherwise. The angles of emerging crack patterns have been evaluated using the software Inkscape 1.3.2. All determined angles are considered to have an error of $\pm 0.2°$.

Each of the examples is presented in the corresponding subsection below. The thickness of the specimens is considered as 1 mm unless stated otherwise.

3.1 Single Edge Notched Tension

A single-edged notched tension specimen is considered in this section to compare the crack propagation with the experimental investigation. The experimental res-

P_{21}^+	P_{21}^-	P_{22}^+	P_{22}^-	α
0.3	0.25	0.225	0.225	0

Table 4: Puck failure properties.

$G_{C,f}\left(\frac{N}{mm}\right)$	$G_{C,m}\left(\frac{N}{mm}\right)$	ζ_f	ζ_m
106.3	0.7879	5	1

Table 5: Multi-phase field properties.

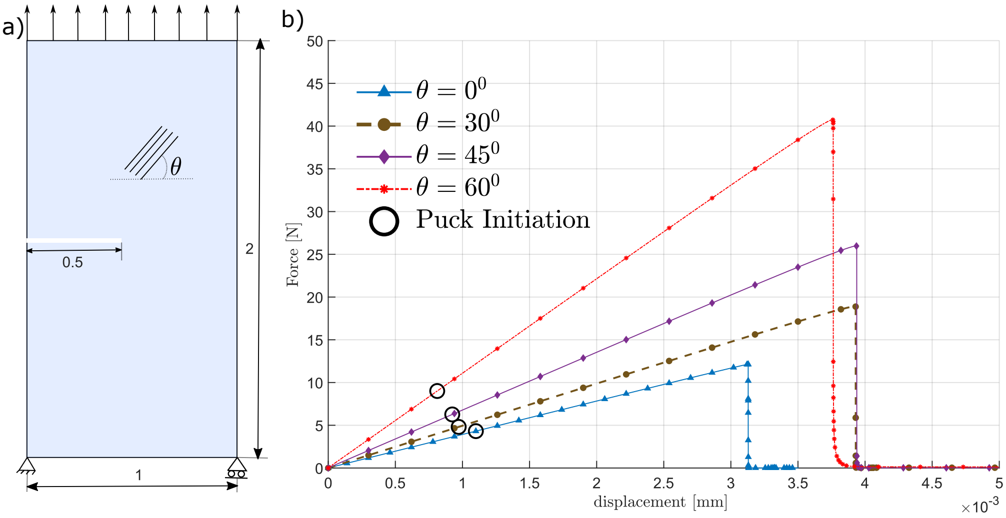

Figure 2: a) Geometric description of the plate with the notch, b) force-displacement curves along with Puck initiation for the fiber orientations of 0°, 30°, 45°, and 60°. All lengths are given in mm.

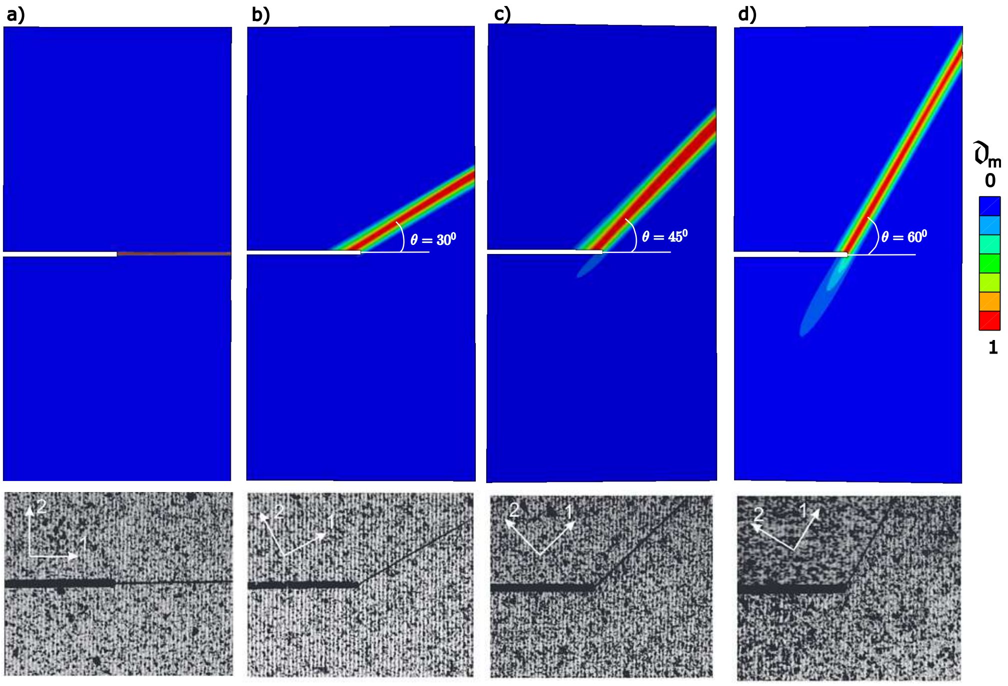

Figure 3: Comparison between experimental results from [3] and the present model in terms of crack propogation for the fiber orientations of a) $\theta = 0°$, b) $\theta = 30°$, c) $\theta = 45°$, and d) $\theta = 60°$.

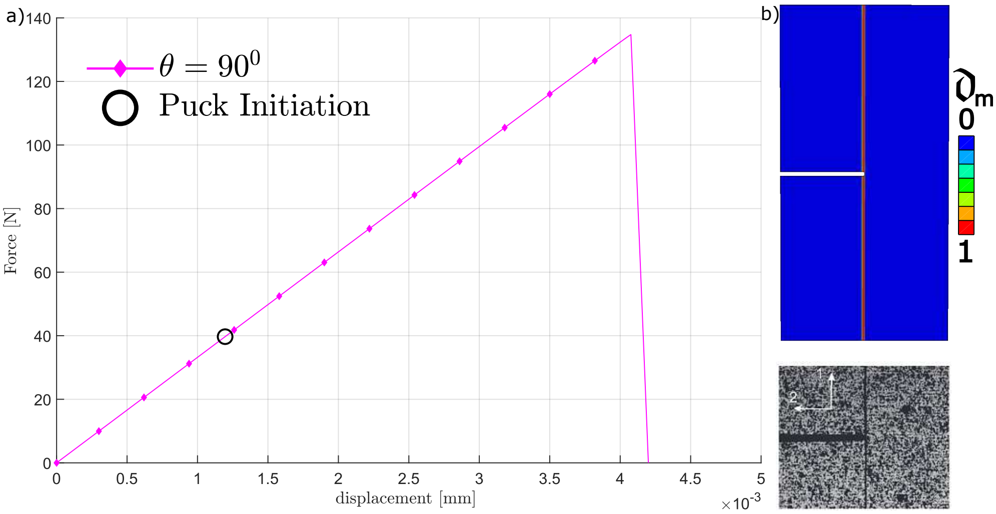

Figure 4: a) Force-displacement curve along with the Puck failure initiation for fiber orientation of 90°, b) comparison between experimental results from [3] and the present model in terms of crack propagation.

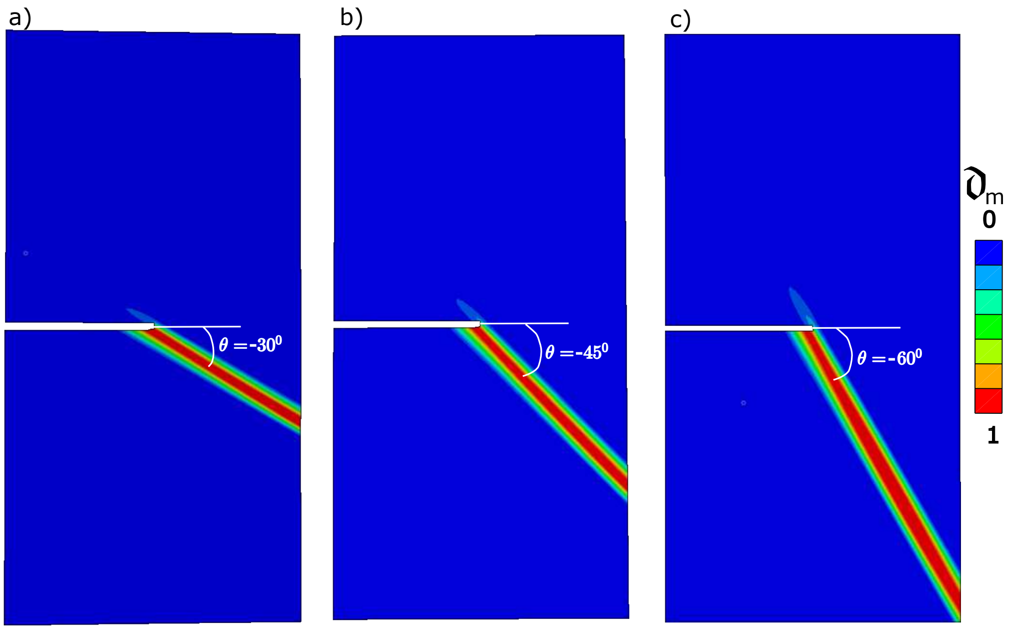

Figure 5: Crack propagation for the fiber orientation of a) $\theta = -30°$, b) $\theta = -45°$, and c) $\theta = -60°$.

ults are taken from [3]. The example consists of a plate of dimension 1×2 mm with an edge notch, with fibers oriented at an angle θ with respect to the global x-axis as shown in figure 2 a). The thickness of the specimen is taken as 1 mm The bottom of the plate is fixed in y-direction, with one point at the bottom left edge fully restrained. The displacement load is applied on the top surface as shown in figure 2 a). No restriction is applied to the displacement in the horizontal direction at the top of the specimen. The purpose of this benchmark example is twofold. The simulations compare the crack propagation path and the load reaction for different plies with their fiber orientation varying from $-60°$ to $90°$. The material properties are considered as in tables 2 - 5 in line with the experimental results in [3].

The numerical experiments regarding the single edge notched tension specimen are also presented in [27, 30–33]. Figure 3 presents the crack path observed in the experiments and the present model. The crack path can be seen running along the fiber orientation, leading to a matrix cracking. Furthermore, all the cracks are observed to grow in an unstable manner. The numerical results presented are in good agreement with the experimental observations. Prior studies, as in [30, 31], reported that the fiber orientations with $\theta = 90°$ are proven challenging due to the sharp turn and likelihood of the crack propagating both upward and down-

Fiber Orientation	0°	30°	45°	60°	90°
Experimental results [3]	0	30	45	60	90
Cahill et al. [3] (XFEM)	0	29	43	57	83
Zhang et al. [30]	0	29	43.6	57.5	87
Ishank et al. [31]	0	28.2	42.5	56	85.4
Pranavi et al. [32]	-	29	42	55	-
Mrunmayee et al. [27]	-	27.3	42.7	57	-
Hrishikesh et al [33]	0	27.5	42	57	-
Present model	0	30.35	46.18	60.40	90

Table 6: Comparison of the crack propagation angle between the present framework and the other available methods in the literature.

ward. Consequently, the numerical crack propagation path in the related literature showed a deviation between $3° - 8°$ from the experimentally observed results. The results obtained from the proposed model for the $\theta = 90°$ case are presented in figure 4 b). It can be seen that the numerical model accurately describes the experimental results even for the fiber oriented at $\theta = 90°$. The force-displacement graphs for $\theta = 90°$ is presented in figure 4 a), whereas for the $\theta = 0°$ to $\theta = 60°$ is presented in figure 2 b) along with the Puck initiation. The comparison between the presented model and the other available models in the related literature is presented in table 6. The angles are measured from the center, where the Phase-field value is dense in an undeformed configuration. Furthermore, figure 5 presents the crack propagation for fibers oriented at $\theta = -30°$, $\theta = -45°$, and $\theta = -60°$. Force-displacement results for the negative fiber orientation coincide with their positive counterpart. Hence, they are omitted for the sake of brevity.

3.2 Open-Hole Tension

The second example aims to show the responses of open-hole specimens to tension. The experimental results for the open-hole tension test are taken from [38]. The experimental results are presented for the fiber angles of $\theta = 0°$, $\theta = 45°$, and for $\theta = 90°$ whose dimensions differ from each other as each specimen with different fiber orientation had different dimensions in the experiments. As a consequence, this section is divided into two parts: (a) Comparison to the experiment [38] is shown in section 3.2.1 and (b) generalized results shown in section 3.2.2 to understand the effect of the fiber orientation.

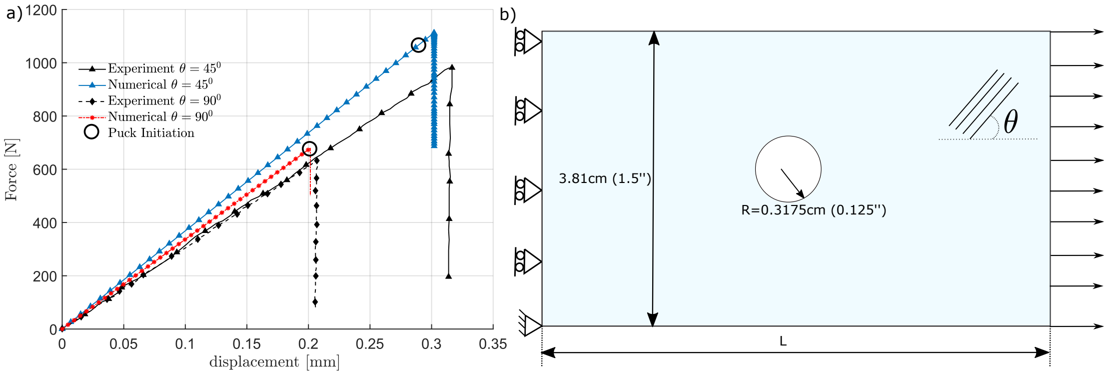

Figure 6: a) Force-displacement curve comparison for the Open hole tension between the experiment [38] and the present model. b) Geometrical description of the open hole tension specimen for comparison with the experiment

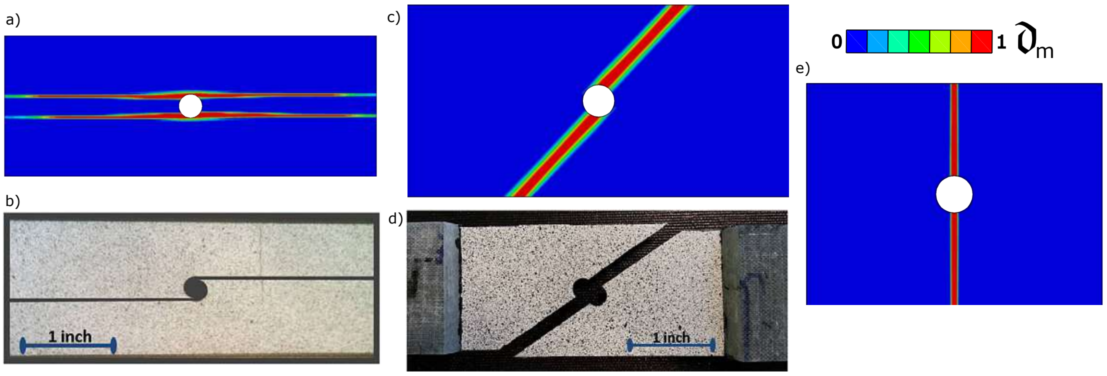

Figure 7: Comparison with the experiments for the open hole tension. Numerical results for a) $\theta = 0°$, c) $\theta = 45°$, and e) $\theta = 90°$. The experimental results [38] for b) $\theta = 0°$, and d) $\theta = 45°$.

E_{11} (MPa)	E_{22} (MPa)	ν_{12}	ν_{21}	G_{12} (MPa)
136000	4670	0.011	0.33	3200

Table 7: Elastic Properties of the open-hole tension test with comparison to the experiment [38].

R_{11}^T (MPa)	R_{22}^T (MPa)	R_{12} (MPa)
2142	42.5	90

Table 8: Strength properties of the open-hole tension test with comparison to the experiment [38].

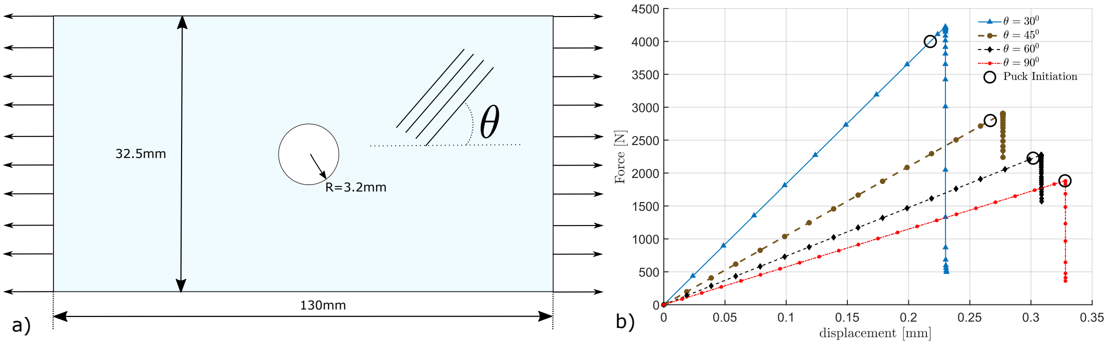

Figure 8: a) Geometrical description of the open hole tension specimen for generalized OHT. b) Force-displacement plots along with the Puck failure initiation for the fibers oriented at angle $\theta = 30°$, $\theta = 45°$, $\theta = 60°$, and $\theta = 90°$.

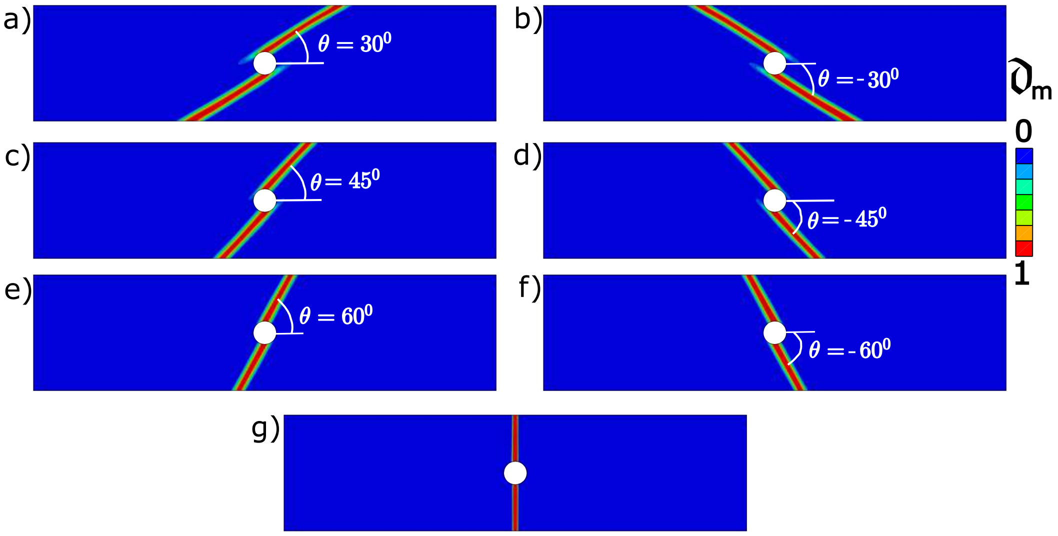

Figure 9: Crack propagation in open hole tension for the fiber angles of a) $\theta = 30°$, b) $\theta = -30°$, c) $\theta = 45°$, d) $\theta = -45°$, e) $\theta = 60°$, f) $\theta = -60°$, and g) $\theta = 90°$

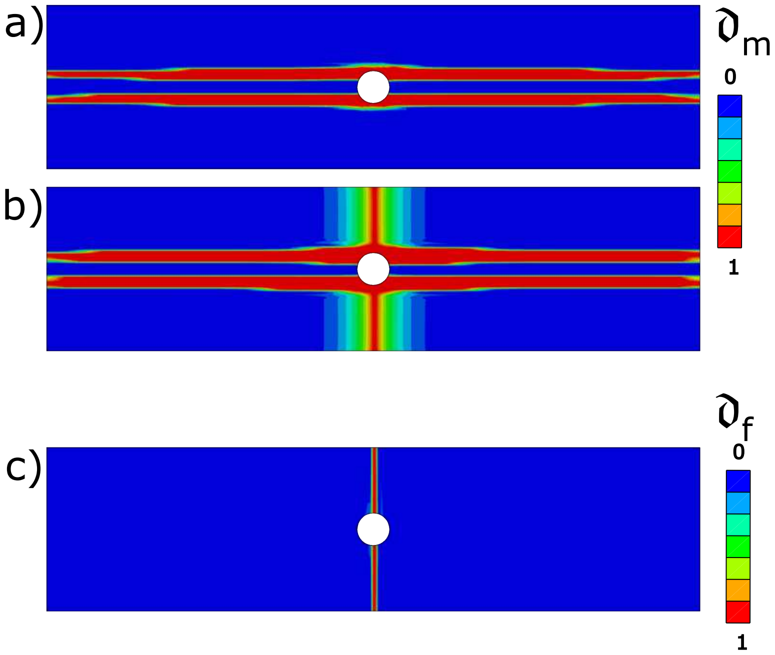

Figure 10: Crack propagation in the open hole tension for the fiber angle of $\theta = 0°$. a) Matrix damage pattern shortly before fiber damage initiates, b) matrix damage pattern after full fiber failure, and c) fiber damage pattern after full fiber damage.

$G_{C,f}\left(\frac{N}{mm}\right)$	$G_{C,m}\left(\frac{N}{mm}\right)$
81.5	0.67

Table 9: Multi-phase field properties of the open-hole tension test with comparison to the experiment [38].

3.2.1 Comparison with the experiments

The material properties are considered as in tables 7 to 9 in line with the experiment [38]. The problem of open hole tension has been addressed numerically also in [26, 27, 30, 39–41]. Figure 6 b) presents the geometrical description of the specimens. Furthermore, the geometry width is always kept constant at 3.81cm or 1.5". The length L is taken as $L = 5.08$cm (2" inch) for $\theta = 90°$, $L = 7.62$cm (3" inch) for $\theta = 45°$, and the $L = 10.16$cm (4" inch) for $\theta = 0°$ according to the experiment [38]. Figure 6 a) compares force-displacement curves between the experimental results and the proposed model along with the Puck initiation, while figure 7 compares the crack propagation path with respect to the experimental observation. For the ply with the orientation of $\theta = 45°$, the numerical results show a propagation angle of $\theta = 45.64° \pm 0.25°$ in line with the experimental results. For the $\theta = 90°$, the experimental results are partially provided in [38] with no picture of the experimental observation. Hence, only results stemming from the numerical results are presented. A similar pattern of crack propagation can also be seen in [39]. For the case with fibers orientated horizontally, i.e., $\theta = 0°$, the crack propagation has an equal probability of propagating from both top and bottom of the hole. Consequently, the numerical results show both possibilities. In conclusion, the force-displacement curve in figure 6 b) and crack propagation in figure 7 show excellent co-relation both qualitatively and quantitatively with the experimental observations.

3.2.2 Generalized Open Hole tension

In order to standardize the results stemming from open-hole tension, a general geometry is used. Figure 9 a) shows the geometry under consideration taken from [12]. A symmetric boundary condition consisting of a prescribed displacement along the x-coordinate on the left and right edges of the plate is investigated. Within this context, eight different fiber directions are considered, i.e. fibers with orientation of 0°, 30°, 45°, 60°, 90°, −30°, −45°, and −60°. The domain is discretized by 12712 4-node quadrilateral plane stress elements. Each of the following examples considers a length scale associated with matrix failure of $\ell_m = 4$ mm and a length scale associated with fiber failure of $\ell_f = 8$ mm, while the rest of the properties are as presented in tables 2 - 4.

The results for the matrix phase field of these numerical experiments are shown in figure 10. The actual propagation angles for 30°, 45°, 60° fiber orientations are measured to be 31.9°, 46.18°, 60.56° with an error of ±0.2°. Besides the case where the fibers coincide with the horizontal direction, all cases exhibit purely matrix-dominated cracking behavior where only the matrix is damaged parallel to the fiber direction with no activation of fiber failure. For the 0°-case, the matrix fractures along the fiber direction starting from the top and the bottom of the open hole. Furthermore, clear fiber failure occurs starting from the top and bottom of the hole and extending to the domain's upper and lower boundaries. Lastly, the matrix gets damaged in the areas where fiber failure is present, as seen in figure 8.

The force-displacement behavior of each numerical example is obtained by summing up all the reaction forces in the global x-coordinate on the displaced boundaries. Again, the behavior of the 0°-case differs from the other cases due to the fiber failure. All cases except the 0°-case exhibit unstable crack growth, indicated by the sharp drop in reaction force once the crack has formed. This can be observed in figure 9 b). Furthermore, the force-displacement behavior is linear until a fracture happens with unstable crack propagation immediately following the Puck matrix failure initiation. Additionally, the displacement at breakage decreases with decreasing fiber orientation angle while the maximum force at damage increases. This is due to the fiber becoming increasingly important at lower ply angles. It is also interesting to note that, as the fiber orientation change from 90° to 30°, the delay between Puck failure initiation and unstable crack propagation increases. Specifically, for the fiber orientation of 90°, the puck failure initiation is immediately followed by an unstable crack propagation, while for the fiber orientation of 30°, the Puck failure initiation is followed by a small nucleation phase before unstable crack propagation as in Fig 8b).

3.3 Compact Tension

This example aims to show a comparison between the experimental and the numerical results in terms of the crack propagation path to compact tension specimens subjected to symmetric loading conditions. The experimental results presented in this section are mainly from the Institute of Polymer Product Engineering, Johannes Kepler University, Linz, Austria. Consequently, details regarding the experimental setup are omitted in the thesis. The geometry under consideration as in the experimental setup is presented in figure 11 a), with a thickness of 5.5 mm. A symmetric loading is applied to the top and bottom surface via the holes using the clamps as in figure 12 b). The experiments consist of unidirectional plies, each of thickness 0.125 mm, stacked on top of each other. Three different orientations of 0°, 45° (considered as $-45°$ as per the previous numerical convention), and 90°. The crack propagation path in the experiments for the fiber orientation of 0°, 45°, and 90° are presented in figure 12 b), d) and f), respectively. It is also evident from figure 12 that the crack propagation follows the path of the fiber orientation. Consequently, this led to an inter-fiber-dominated failure. Similar results for the experiments on the compact tension for the fiber orientations 0° and 90° of can be found in [42].

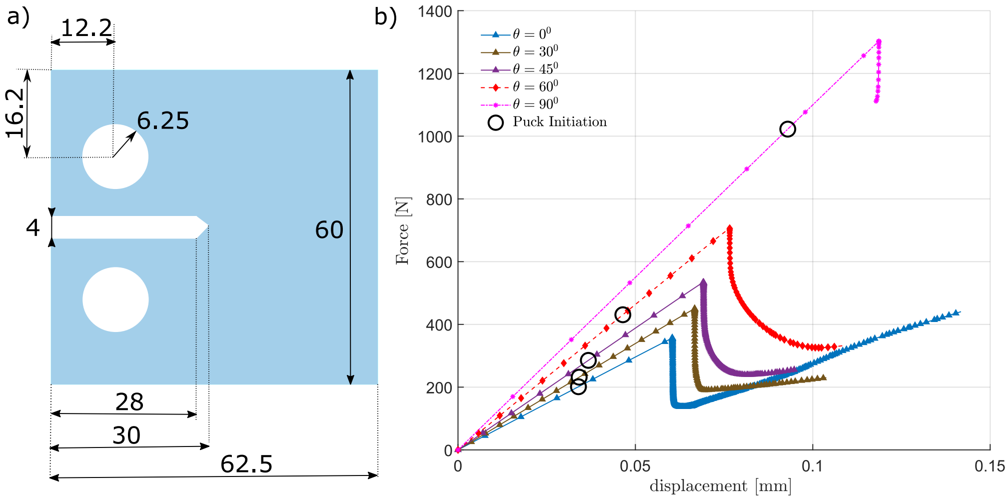

Figure 11: a) Geometrical description of the compact tension specimen, and b) force-displacement curve along with the Puck failure initiation for the fiber orientations of 0°, 30°, 45°, 60°, and 90°. All lengths in a) are considered to be in mm.

The numerical results concerning the compact tension utilize the material properties as in tables 2 - 5. Due to the dimensions of the experimental specimen, the length scale associated with matrix failure is considered as $\ell_m = 2.5$ mm and the length scale associated with fiber failure as $\ell_f = 5$ mm. Furthermore, the numerical model is meshed with 36947 elements to map the structure accurately. Figure 11 a), c) and e) presents the comparison of the crack path for the fiber orientations of 0°, 45°, and 90° respectively. The crack propagation path obtained in the numerical results is measured as 0°, $45.40° \pm 0.2°$, and 90° respectively. The results show the ability of the model to accurately describe the crack propagation path compared to the experimental results. Furthermore, for the case with fiber orientations of 90°, the experimental results shows crack propagation upwards as in figure 12 f), while the numerical results show the crack propagation in both upward and downward directions. This could be due to two main factors: a) the asymmetrical notch due to machining arising from the experimental setup, and b) the probability of the crack taking the path. The experimental results of the multiple samples show that the crack propagation is sometimes upward and sometimes downward. Consequently, the numerical model considers both possibilities of crack propagation in samples with fiber orientation of 90°. Furthermore, figure 13 presents the crack propagation for the fiber orientations of $-60°$ to 60°. In all cases, interfiber-dominated failure is observed. Figure 11 b) presents the force-displacement curves for fiber orientations of 0° to 90° along with the Puck initiation. It can be easily observed that as

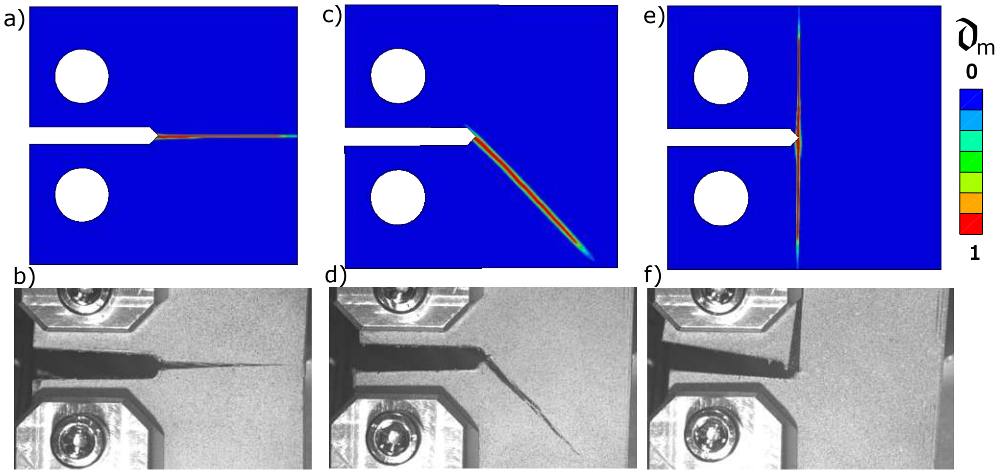

Figure 12: Comparison between the experimental observation (courtesy of Prof. Zoltan Major, Johannes Kepler University, Linz, Austria) and present model of the crack propagation path in compact tension for fiber orientation of a) and b) 0°, c) and d) 45°, as well as e) and f) 90°.

the fiber orientation increases, the apparent strength of the composite structure increases. For the fiber orientations close to 90°, the strength of the structure increases, leading to more fracture resistance.

3.4 Centre Notched Tension

This example shows the model's ability to predict crack propagation and compares them with the experimental results for the center-notched tension plate. The experimental results are presented in [3]. The geometry, excluding the clamps for the mounting, consists of the Length of $L = 48$mm and the width of $W = 25$mm. The notch is placed at the center of the plate, and its width is 9.6 mm. Numerically, only the geometry without clamps is modeled. The geometry is modeled with 15524 elements. The bottom part of the plate is completely fixed, while the displacement boundary conditions are applied at the top boundary. The material properties are taken as in tables 2 - 5 in line with the experimental setup [3], whereas the length scales for the matrix and the fibers are considered as $\ell_m = 10$ mm and $\ell_f = 4$mm, respectively. Figure 14 presents the comparison of the crack path with the experimental observations for the plies with fiber orientations of 0°, 30°, 45°, 60°, and 90° in the same order as mentioned here. Furthermore, the actual angles of the crack prorogation stemming from the numerical results are estimated as 0°, 29.85°±0.2°, 44.52°±0.2°, 59.85°±0.2°, and 90° respectively. All failure mechanisms are flagged

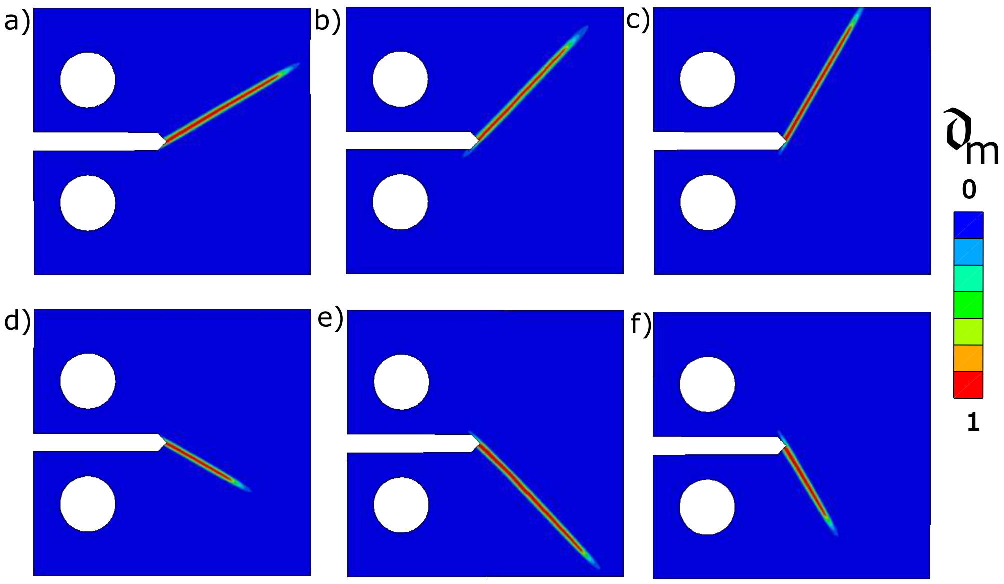

Figure 13: Crack propagation in compact tension specimen for the fiber orientation of a) 30°, b) 45°, c) 60°, d) −30°, e) −45°, and f) −60°.

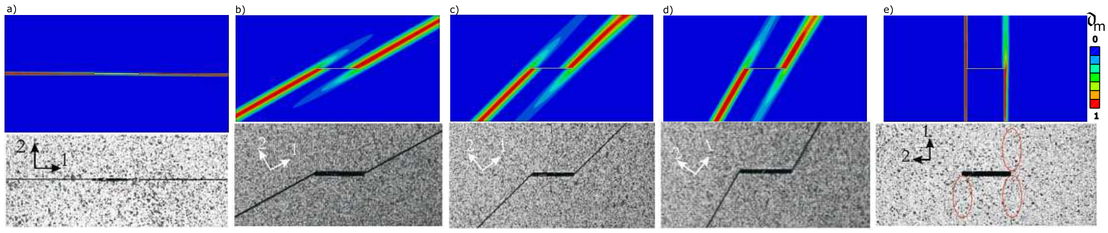

Figure 14: Comparison between the experimental observations from [3] and the present model for the fiber orientations of a) 0°, b) 30°, c) 45°, d) 60°, and e) 90°.

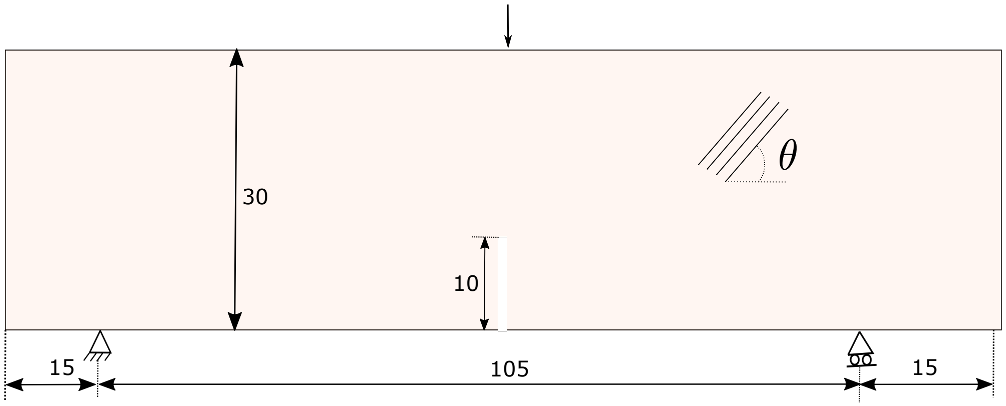

Figure 15: Geometrical description of the three point bending sample. All lengths are considered to be in mm.

as matrix dominated failure. Consequently, the length scale corresponding to the fiber does not play any role. For the fiber with the orientations of 90°, experimental investigation as in figure 14 e) suggests that the likelihood of crack propagating from both sides is equal. Furthermore, the crack is likely to travel symmetrically up and down. Within this context, only one crack travels and reaches the top and bottom clamping surface, and the other crack only propagates either top or bottom. The numerical observations presented in figure 14 e) also match the experimental observation. Force vs reaction is not given for the centre notched tension specimens for brevity reasons. However, it has been observed that the force vs reactions follow a pattern to that in single edge notched tension specimens.

3.5 Three-point Bending

This section is aimed to show the crack propagation in a three-point bending specimen. Again, the simulation is done with the eight different ply angles as in sections 3.1 and 3.2. All calculations use the same geometry and discretization. The geometry consists of a unidirectional composite ply with a length of $L = 145$ mm and a width of $S = 105$ mm. A notch is placed with a length of one-third of the height of the specimen. Furthermore, the bending beam is supported by two supports, where the left support is a fixed and the right support is a floating bearing. A displacement at the top of the beam with is applied with a width of 5 mm. Figure 15 presents the geometric description and boundary conditions. 20736 elements discretize the domain. The material properties are taken as in tables 2 - 5 with $\ell_m = 4$mm and $\ell_f = 8$mm. A similar analysis for three-point bending using a phase field model has been carried out in [43].

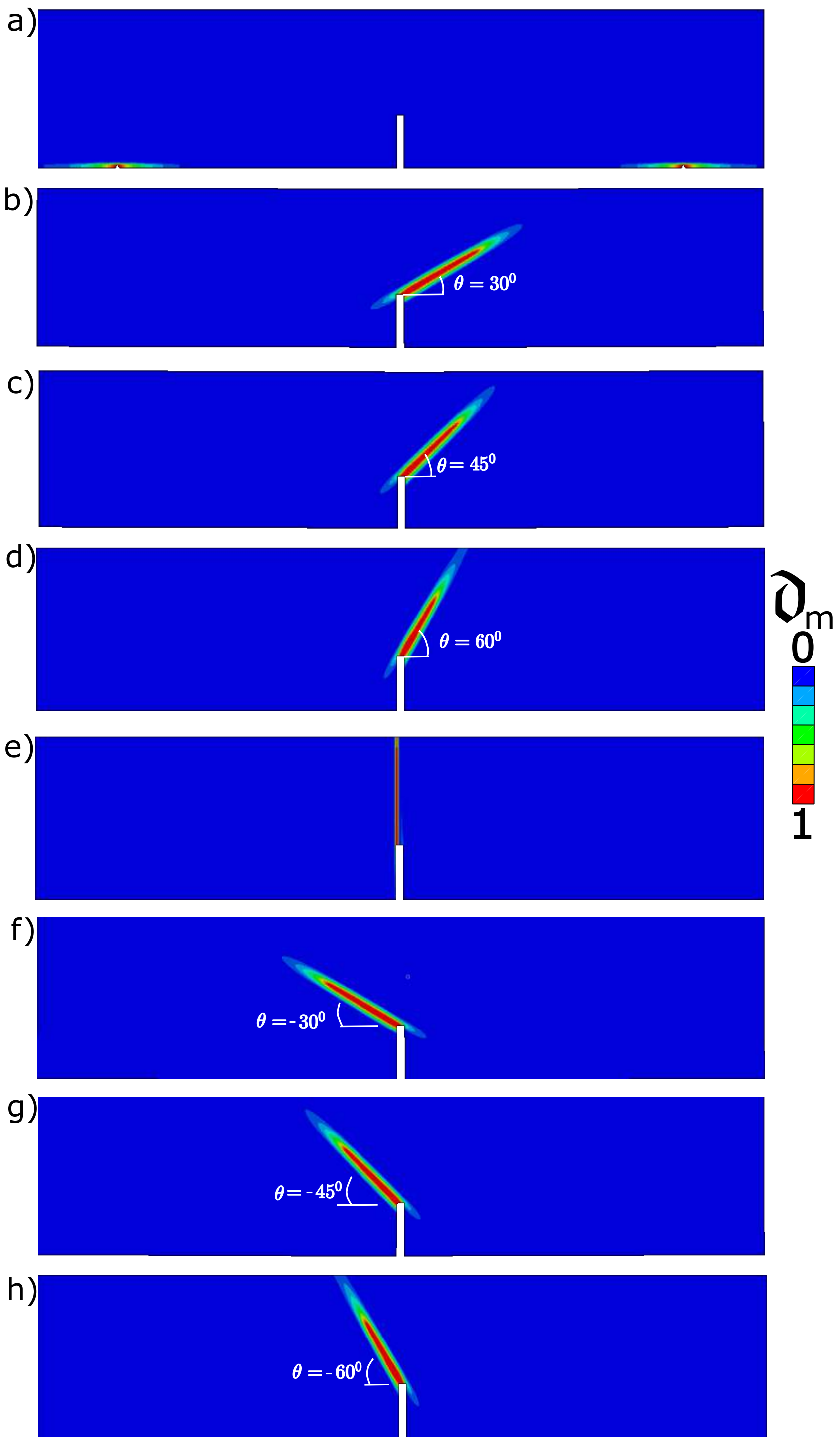

Figure 16: Crack propagation in three-point bending specimen with fiber orientation of a) 0°, b) 30°, c) 45°, d) 60°, e) 90°, f) −30°, g) −45°, and h) −60°.

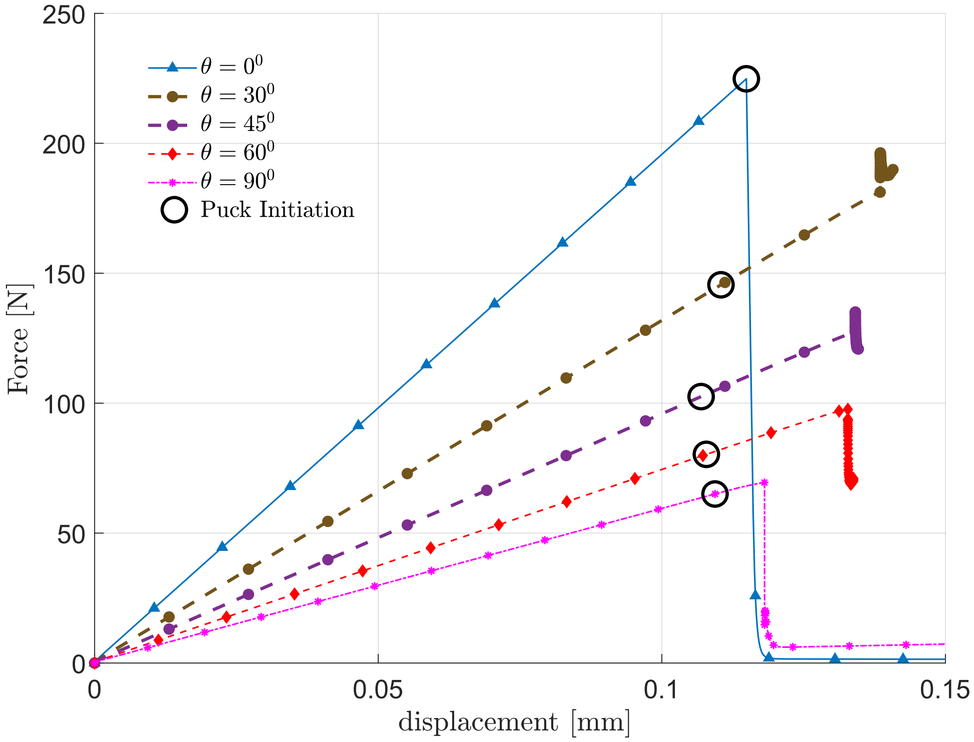

Figure 17: Force vs displacement along with the Puck initiation for the three-point bending specimen for the fiber orientation of 0°, 30°, 45°, 60°, and 90°.

In the present numerical simulation, it is observed that failure occurs in the vicinity of the supports. Therefore no crack propagation is found for the case with a fiber orientation of 0°. Figure 16 a) shows the damage at the supports. Furthermore, for the fiber orientation of 30°, 45°, −30°, and −45°, crack propagation patterns as shown in figure 16 b), c), f) and g), respectively, are obtained. After the damage patterns depicted in figure 15 emerge, additional cracks start to nucleate in the vicinity of the load application. This leads to abrupt changes in the force vs displacement behavior. Consequently, only the results until this point are considered for the simulation. This could be due to the low matrix strength compared to the fibers. As a consequence, this leads to damage at the boundary conditions. As a workaround, boundaries with an increased fracture energy can be considered. Figure 16 d), h) and e) presents the three-point bending for the fiber orientations of 60°, −60°, and 90°. No failed boundary issues are found in these cases. Figure 17 presents the force vs displacement curve for the three-point bending specimen for various fiber orientations along with their Puck initiation. As the angle of the fiber increases, the structure's load-bearing capacity decreases. This is due to the definition of the fiber orientation angle and the load application direction of the fiber orientation in the geometric description.

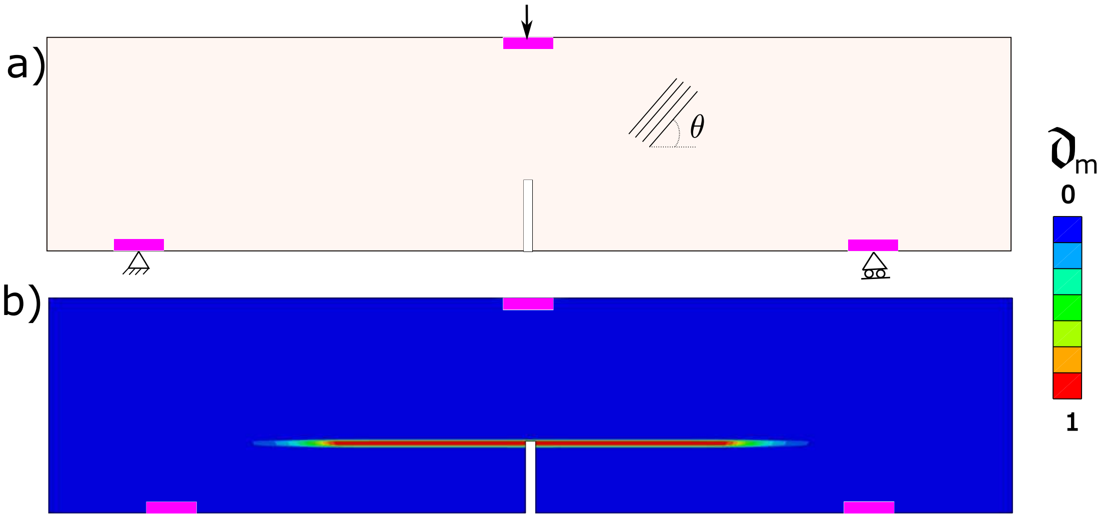

Figure 18: a) Boundary conditions of the reinforced three-point bending specimen. b) Crack propagation in reinforced three-point bending specimen with fiber orientation of 0°.

Furthermore, in order to simulate the crack propagation in the ply with fiber orientation of 0°, the aforementioned sections with increased fracture energy are introduced at the boundaries as in figure 18 a). The crack propagation due to the

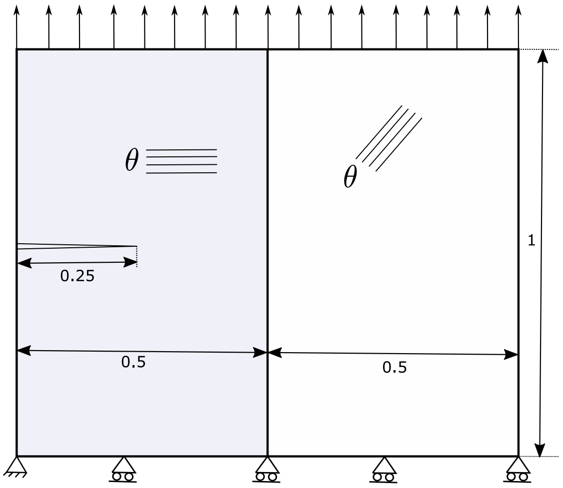

Figure 19: Geometrical description of the bimaterial system specimen. All lengths are considered to be in mm.

stiff boundaries is presented in figure 18 d) with fiber orientation of 0°. The results show that the crack forms horizontally as the load increases, leading to stable crack propagation until the crack propagates the whole width of the structure.

3.6 Bimaterial System

This section aims to show the present model's predictive capability to handle interfaces between two different fiber orientations. For this purpose, a unit square with a notch is divided into two segments. A depiction of the problem, including its boundary condition, can be seen in figure 19. The left segment is always set up to have a fiber orientation of 0°, while the right side has different fiber directions for each case as in [32]. These fiber directions are 30°, 45°, 60°, 90°, −30°, −45°, and −60°. The same discretization and boundary conditions are used for each case, with the domain being discretized by 20306 elements. The material properties are different to the ones in tables 2 and 3 with the elastic properties being $E_{11} = 171000$ MPa, $E_{22} = 9080$ MPa, $G_{12} = 5390$ MPa and $\nu_{12} = 0.0169$. The strength properties are set to $R_{11}^T = 2323.5$ MPa, $R_{22}^T = 62.3$ MPa, $R_{11}^C = 1200.1$ MPa, $R_{22}^C = 199.8$ MPa and $R_{12} = 92.3$ MPa. The properties relating to Puck failure are the same as in table 4. Lastly, the multi-phase field properties are changed to $\ell_f = 0.1$ mm, $\ell_m = 0.05$ mm, $G_{C,f} = 81.5\ \frac{N}{mm}$ and $G_{C,m} = 1.2774\ \frac{N}{mm}$ while the rest of these properties remain unchanged. A similar example for the bimaterial system and multiple interface problems has been presented in [32], where a traction separation law is used at the interface to model the interface between the two fiber

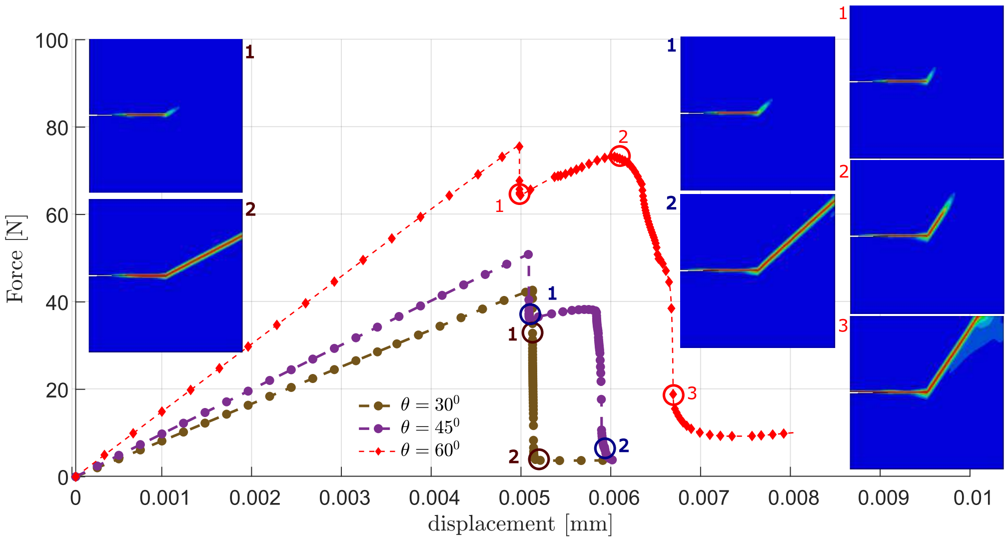

Figure 20: Force vs displacement plots for the bimaterial system with crack propagation for the fiber orientation of 0/30°, 0/45°, and 0/60°.

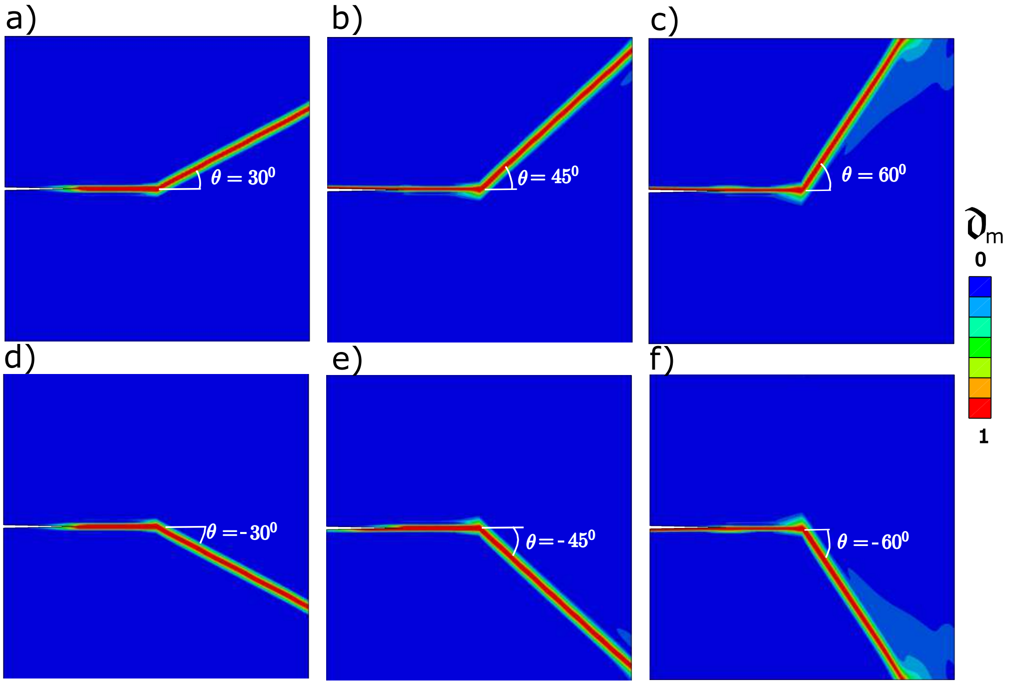

Figure 21: Crack propagation in the bimaterial system for the fiber orientation of second layer of a) 30°, b) 45°, c) 90°, d) −30°, e) −45°, and f) −60°.

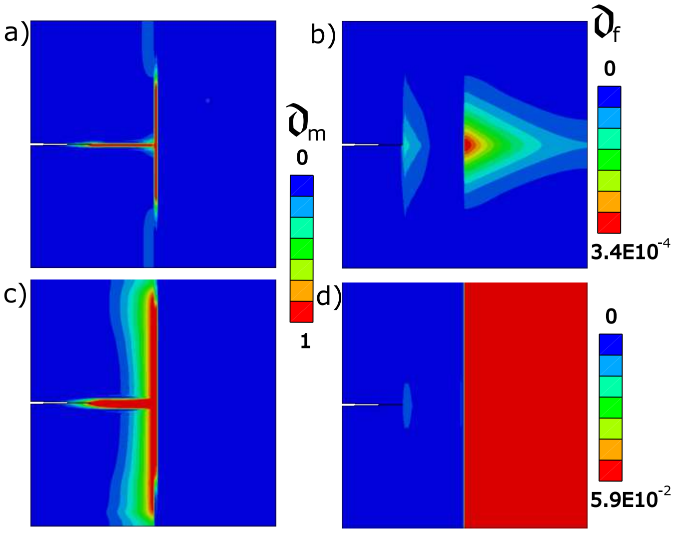

Figure 22: Crack propagation of the bimaterial system with fiber orientation of 90°, along with the interplay between the fiber and matrix failure.

parts of the domain. The present work shows that the presented model can be used directly without any cohesive zone model. Within the context of [32], the work in this present model considers a perfect interface. In contrast, soft interfaces would need an extra layer between the left and right domains with reduced fracture toughness.

The matrix damage plots for all cases except 90° are shown in figure 21. All cases exhibit a matrix crack along the different fiber directions, showing that the present implementation is able to predict the behavior of interfaces without further modifications. Furthermore, when the crack hits the interface, it is immediately deflected to the fiber orientation of the right side of the domain. This is due to the bonded interface leading to the change of material orientation at the interface. Similar kinking can also be observed in [32]. For the fiber orientations corresponding to 90°, the interaction between the matrix damage and fiber damage can be clearly seen in figure 22. Within this context, first, the matrix fails in the left domain and propagates to the interface. As soon as the crack hits the interface, the crack starts to propagate upwards, following the fiber direction of the right domain as presented in figure 22 a). Furthermore, fiber damage is initiated at this point. Consequently, the first occurrence of fiber damage can be seen in figure 22 b). As the crack progresses, it becomes thicker as a consequence of the boundary, further increasing fiber failure in the right side of the domain as shown in figure 22 c) and d). At this point, all the fibers in the right domain are equally in damaged due to a fully formed crack along the interface leading to the body being practically split into two parts. No complete fiber damage is observed as the crack hits the boundary before complete fiber damage.

Figure 20 shows the force-displacement curves for fiber orientations of 30°, 45°, and 60°. All cases exhibit linear elastic behavior at first, followed by a sudden drop in the reactions as soon as the crack starts to propagate towards the interface. For each case, a color-coded map of the crack hitting the interface and the corresponding load drop in the force vs displacement is presented in figure 20. The cases with fiber orientations of 45° and 60° exhibit higher stiffness which is expected given the loading direction. These cases show a stable crack propagation for a while before becoming unstable again when the crack is close to the boundary. Furthermore, the fibers with orientations of ±30° show completely unstable crack propagation, leading to a further drop in the force as shown in figure 20. The Puck matrix damage initiation happens for all cases at approximately 0.0012 mm of displacement.

For the force in the 90° case, after an initial linear behavior, a slight drop in force can be observed when the crack hits the interface. This crack continues to grow towards the upper and lower boundaries after this point. Since no complete fiber failure is obtained, the fibers in the right half of the structure can sustain the majority of the load, leading to an increased force with no significant drop in reaction force even though the structure is completely broken judging by the matrix damage in the left domain.

3.7 Tension in Unnotched Specimens

Carbon fiber-reinforced polymers are prone to defects. The defined variability from the nominal flat laminate is often classified as a defect. See [44] for more details. The fiber defects can occur due to misalignment, in-plane and out-of-plane fiber undulations, and folds of the plies in fiber or transverse to fiber directions. Furthermore, fiber defects depend highly on the fiber architecture [44]. At the same time, matrix defects stem from porosity or starved areas, dry spots, and fiber washouts [45]. The studies regarding the defects suggest a reduction of 10% in strength due to fold defects [46–48]. The effects of voids, fiber washouts, and locally compacted regions can be found in [49, 50] and the references therein.

Consequently, this example aims to show the intricate nature of the formation of cracks in the specimens without any stress concentrations. Under these conditions, the crack first develops microscopically, followed by a coalescence. These small cracks coalesce forming a larger crack followed by propagation of damage. Under such circumstances, the crack path can only be entirely determined if the statistical data regarding the internal flaws of the stricture is available. In order to solve such a system numerically, a few randomly distributed defects are installed in the structure by reducing the fracture toughness at those points by 5 to 10%. Furthermore, Puck failure criteria can already initiate cracks, and the proposed

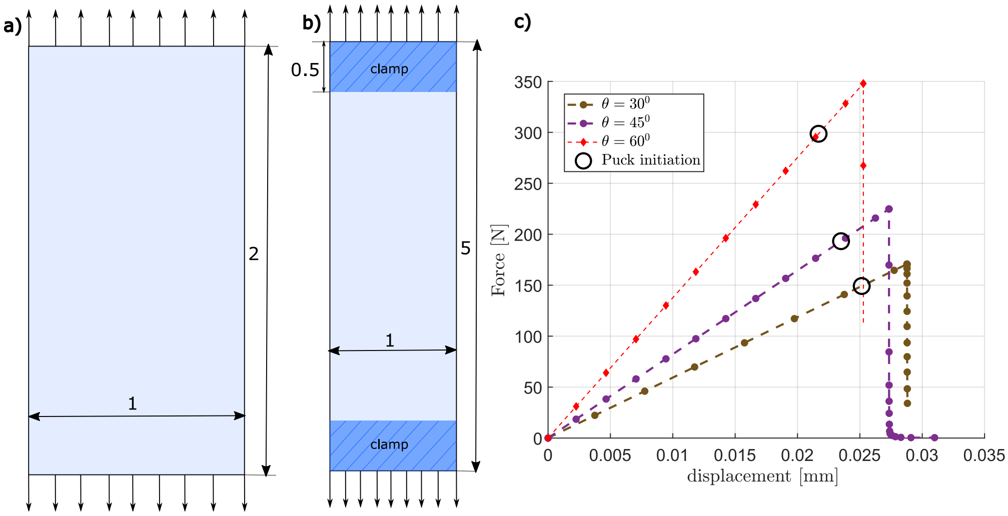

Figure 23: a) Geometric description of the tension in unnotched specimen used for the fiber orientation of 0°, and 90°, whereas b) presents the geometrical description for fiber orientations of 30°, 45°, and 60°. All lengths are considered to be in mm.

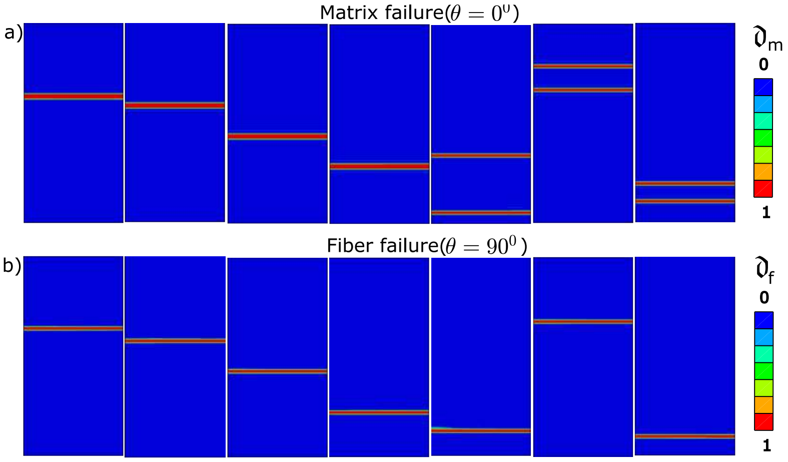

Figure 24: a) Matrix failure in different regions due to different configurations for the fiber orientation of 0°, and b) fiber failure in different regions due to different configurations for the fiber orientation of 90°.

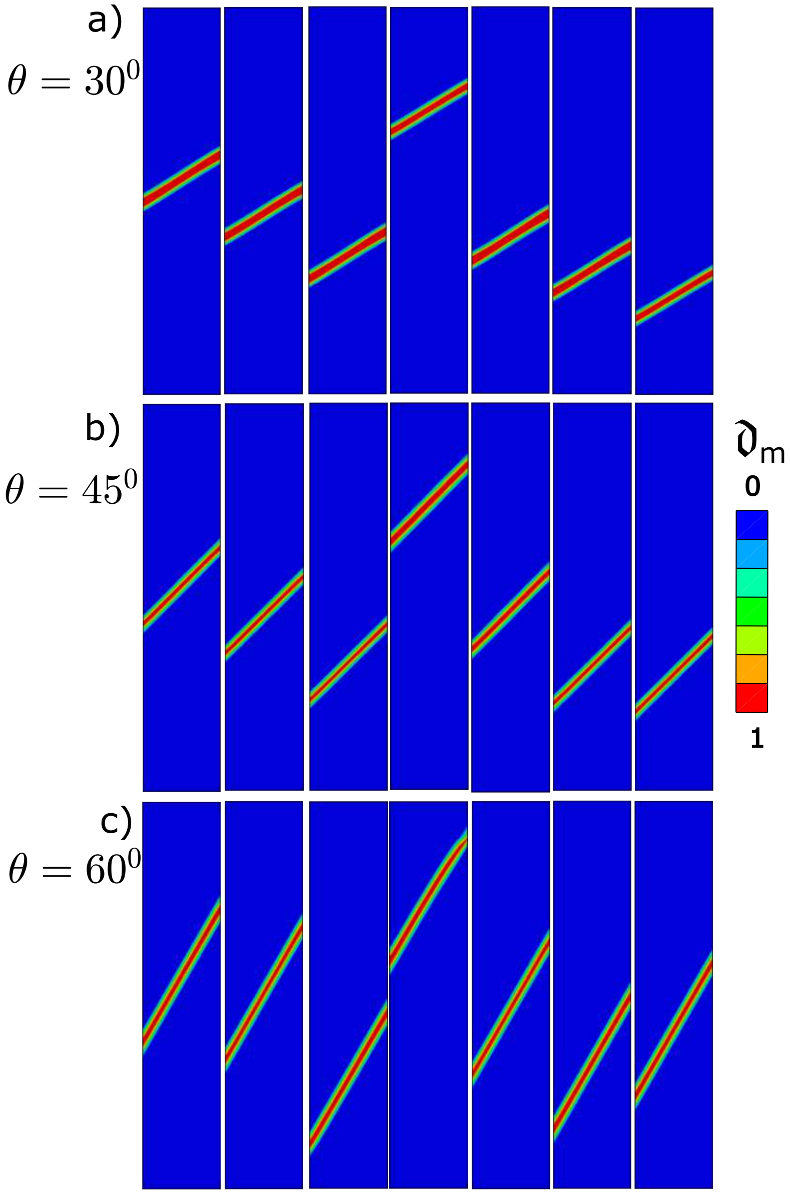

Figure 25: Matrix failure in different regions due to the different configurations of the fiber orientation of a) 30°, b) 45°, and c) 60°.

framework within the phase field can coalescent the cracks and propagate them.

Figure 23 a) presents the geometrical description of the specimen. A pristine plate with fibers oriented in 0° and 90° is used for this example. For the ply with fiber orientation of 30°, 45°, and 60° the geometry in figure 23 a) would always have a crack starting from the boundary. To circumvent these issues and remove the boundary effects in these ply orientations, another geometry with a length of $L = 5$ mm is used. In order to simulate the actual test case, the top and bottom parts of the geometry are filled with material with very high stiffness and fracture toughness. Furthermore, this setting discards cracks originating from the boundary numerically.

Fifteen different random distributions of defects are planted in each model for each case. Each distribution consists of six micro-defects in the form of reduced fracture toughness (5% to 10%). This is achieved numerically by assigning the reduced fracture energy to the corresponding elements obtained from the random distribution. Furthermore, only seven simulations are presented, which show different crack propagation. The nucleation and coalescence for each of the samples are omitted for the sake of brevity. The material properties considered are presented in table 2 - table 5 with length scales taken as $\ell_f = 0.05$ mm and $\ell_m = 0.25$ mm.

Figure 24 a) presents the matrix failure for the fibers oriented in 0°. Seven configurations show the possibility of damage. This is in line with the experimental observations. Furthermore, figure 24 b) presents the fiber failure for the fiber oriented in 90°. Consequently, the load-carrying capacity of the 90° is higher. Additionally, it is noticed that in both cases, the microcracks are formed first, followed by a coalescence between these cracks, with unstable crack propagation concluding the fracture event. Figure 25 a), b) and c) present the different crack paths taken for the fibers with the orientation of 30°, 45°, and 60°. In all these cases, only matrix failure is observed with no fiber damage initiation. The crack path is always parallel to the fibers. Figure 23 b) presents the force vs displacement curves along with the Puck initiation. All the cases show unstable crack propagation. The early onset of the Puck initiation is approximately calculated as 10 to 12% lower than the total load-carrying capacity due to the reduced stiffness of the artificial microcracks in the structure. Furthermore, due to the unstable crack propagation, in all the cases, the difference in the force-displacement curves for different crack paths are almost the same with less than 2% variation in their load-carrying capacity. Hence, only one force vs displacement curve for each fiber orientation is presented for the sake of brevity.

4 Numerical Examples for Laminated Composites

This section shows the capabilities of the current implementation regarding the simulation of laminated composite materials. For this purpose, the mesh overlay method is used to model different laminate layups. The technique itself and its implications for the results are shown in section 4.1. All of the following results are validated with experimental and numerical results. The first set of numerical results concerns itself with a series of coupon tests that have been reported by Flatscher [51]. In these tests, all coupons were laminates with a layup of $[(\theta/-\theta)_8]_s$ with $\theta = 45°$, $60°$, $75°$. The coupons were tested with various loading conditions. These are tensile loading, compressive loading and tensile loading followed by a compressive loading. Only the pure tensile and pure compression results are compared with the current implementation.
The first set of experimental results is an open hole tension test with two different layup sequences [12]. Namely, these sequences concern a cross-ply laminate $[0^\circ_4/90^\circ_4]_s$ and a laminate with the layup sequence $[45^\circ_4/-45^\circ_4]_s$.
The third set of experimental results concern itself with compact tension tests [2] which is outside the capabilities of the mesh overlay method. In their experiments, Li et al. [2] investigated the influence of different layup sequences with the same number of plies and ply directions. Therefore, they experimented with eight different layup sequences, which consisted of four different cross-ply and four different quasi-isotropic layup sequences. The current implementation is compared to two of the cross-ply specimens in section 4.4.

4.1 Mesh Overlay Method

The mesh overlay method is a simple method to replicate the properties of laminated composites in the context of the finite element method in a two-dimensional space. With this in-plane strains can be considered. For this purpose, each node is associated with multiple elements, leading to an overlay of the elements' properties. This means that each element layer represents a ply that experiences the same nodal displacements within the body as all other plies. This leads to multiple plies which show the exact same strains. It is unnecessary to replicate the layup sequences of experiments exactly as all contributions of plies with the same ply angle would lead to the same result as one ply with a higher thickness. As each layer in the mesh overlay method increases the computational cost, multiples of identical plies reduce the number of plies in the layup sequence. These assumptions and reductions lead to computational efficiency. As different layup orders influence the fracture behavior of structures [2], the mesh overlay method itself cannot account

Tests	Layup Sequence	l (mm)	w (mm)
T-45	$[(45°/-45°)_8]_s$	134	32
C-45	$[(45°/-45°)_8]_s$	56	32
C-60	$[(60°/-60°)_8]_s$	32	32
T-75, C-75	$[(75°/-75°)_8]_s$	20	32

Table 10: Length, width and layup sequences of the specimens reported in [51].

for this difference. An additional obvious drawback of the mesh overlay method is that delamination between plies is not modeled, as it is automatically assumed that the bonding between plies is perfect. This leads to differences in comparisons to the experimental results as interply delamination is often reported therein. Since the elements used in the model are plane stress elements, each element has an assigned thickness. With the overlay method, each new overlaid element adds to the total thickness of the laminate. Since all the experiments being used to validate the current implementation are either 2 mm or 4 mm thick, the thickness associated with each ply in the implementation is chosen to be 1 mm. As all simulations need only two different ply orientations per laminate, the total thickness is always 2 mm. The reaction forces are scaled accordingly if the thickness of the experimental specimen is 4 mm.

4.2 Coupon Tests

As mentioned in the introduction to this chapter, five different coupon tests are reported in [51]. The experimental campaign consisted of nine different coupon tests, two of them tensile tests, three compressive tests, and the rest of the specimens being subjected to either tensile followed by compressive loading or vice versa. The latter five tests are not considered for comparison as only monotonic load increases are considered in the compared examples. Table 10 shows the dimensions and layups of the coupons, with l being the free length in the experiments and w being the width of all samples. With a ply thickness of 0.125 mm, all specimens had a total thickness of $t = 4$ mm. The specimens were made of unidirectional Cycom®977-2-35/40-12KHTS-134-300 plies, which is a carbon fiber epoxy laminate. The material properties for the simulations are taken directly from [51] and are shown in tables 11 and 12. As [51] uses different fracture toughnesses in compression and tension, they are shown in table 13 with the superscripts C and T, respectively.

All coupons are discretized with a constant element size of 0.5 mm, which leads to a range of 2560 elements per ply for the T-75 and C-75 coupons to 17152 elements per ply for the T-45 coupon. The boundary conditions are shown in

E_{11} (MPa)	E_{22} (MPa)	ν_{12}	ν_{21}	G_{12} (MPa)
146000	9000	0.02096	0.34	4270

Table 11: Elastic Properties of the composites

R_{11}^T (MPa)	R_{22}^T (MPa)	R_{11}^C (MPa)	R_{22}^C (MPa)	R_{12} (MPa)
2100	82	1407	249	110

Table 12: Strength properties of the elastic

figure 26 a). Similarly to the results shown in section 3.7, the laminated coupons are weakened in a small area by reducing the fracture toughness for both fiber and matrix by 10%, which is in line with experimental observations [46–48]. This leads to a predetermined place for the crack to start. In all the cases, the weakened area consists of four elements in the center of the coupons. Tension or compression is applied to the coupons by displacing both the left and right boundaries, as shown in figure 26 a). Each of the cases are done with the same length scales, as being $\ell_f = 2$ mm and $\ell_m = 1$ mm.

As demonstrated in figure 27, all coupons show matrix dominated cracks without any fiber failure. Each image shows the first increment in which phase-field has been activated. Therefore, complete failure occurs immediately after the Puck initiation in all cases. Consequently, failure occurs in a very unstable way, leading to the phase field showing both crack paths resulting in the x-shaped crack patterns in figure 27. Each of the images in figure 27 is taken at the first occurrence of damage. The resulting damage pattern for the T-45 case is much wider than the other damage patterns. It is perfectly not clear why this happens, but all cases with ±45° orientations show wider damaged areas than other orientations with the same length scales. All force-displacement curves are shown in figure 26 b) for compressive loading and c) for tensile loading. They display the absolute value of the displacement versus the sum of the reaction forces on the right boundary. As plasticity is disregarded in the current implementation, all force-displacement curves are linear until the load limit is reached. Afterwards, unstable crack growth occurs, indicated by the sudden drop in reaction force. Said load limit is compared to the results presented in [51]. Therein, Flatscher lists laminate stresses for each of the compression results by dividing the applied total reaction force F by the

$G_{C,f}^T \left[\frac{N}{mm}\right]$	$G_{C,m}^T \left[\frac{N}{mm}\right]$	$G_{C,f}^C \left(\frac{N}{mm}\right)$	$G_{C,m}^C \left(\frac{N}{mm}\right)$	ζ_f	ζ_m
89.8	0.2	78.3	0.8	1	1

Table 13: Multi-phase field properties

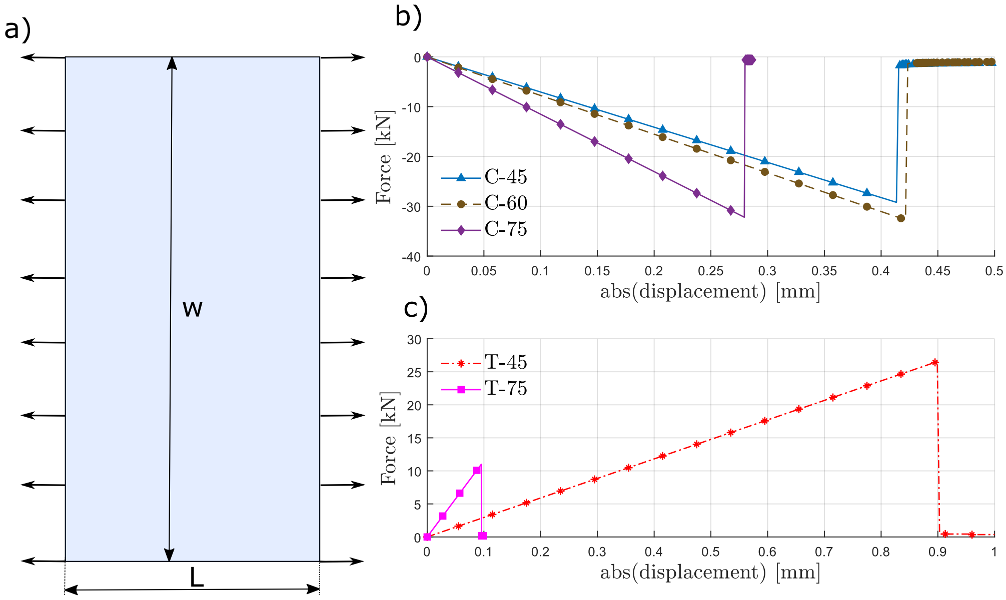

Figure 26: a) Dimensions and boundary conditions for the laminated coupon tests, b) force displacement curves corresponding to the compressive cases and c) force displacement curves corresponding to the tensile tests.

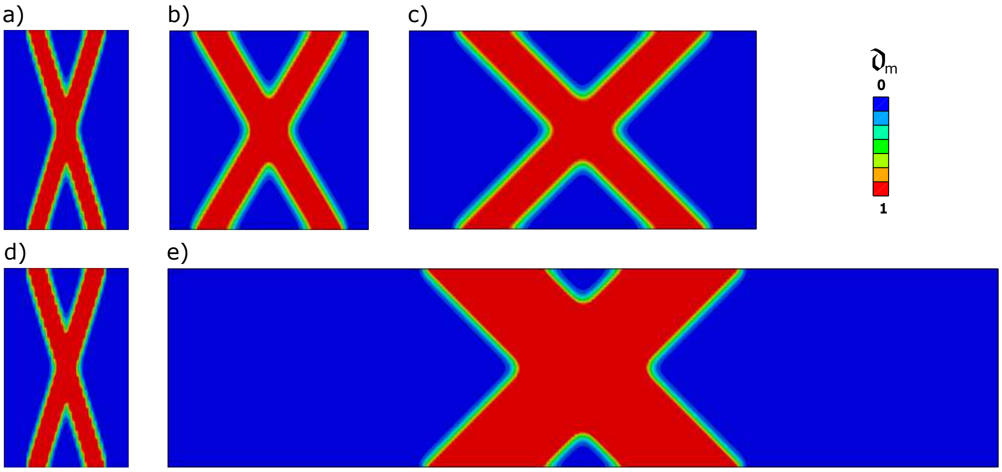

Figure 27: Matrix crack pattern of the coupons for the compressive cases a) C-75, b) C-60, and c) C-75 as well as well as for the tensile tests d) T-75 and e) T-45.

Case	Current Implementation (MPa)	Flatscher [51] (MPa)
C-45	-228.2	-203.1
C-60	-255.7	-198.4
C-75	-251.6	-229.3

Table 14: Comparison of the nominal stress $\bar{\sigma}_{xx}$ determined by the current implementation and the implementation in [51].

nominal cross section.

$$\bar{\sigma}_{xx} = \frac{F}{wt}. \tag{55}$$

The aforementioned comparison is shown in table 14. The current implementation consistently overestimates the predictions by Flatscher, but generally proves to be a good match to these results.

4.3 Open Hole Tension

The open hole tension tests reported by Flatscher et al. [12, 51] use the same geometry and boundary condition described in chapter 3.2.2 which is shown in figure 28. As mentioned above, the laminate sequences investigated herein are $[0^\circ_4/90^\circ_4]_s$ and $[45^\circ_4/-45^\circ_4]_s$. Both specimens consisted of the same material used in the coupon tests in the previous section. Therefore, the same material parameters are used, except for the phase-field driving forces and length scales, which are calibrated to match the experimental results. The length scales are also different between these two layup sequences as the $[45^\circ_4/-45^\circ_4]_s$ sequence shows much more delicate fracture patterns and needs smaller length scales to capture these patterns accurately. Therefore, much smaller length scales had to be used in order to refine these processes accurately.

$[0^\circ_4/90^\circ_4]_s$

For $[0^\circ_4/90^\circ_4]_s$ case, a rather stiff response is expected because half of the fibers are orientated in loading direction. Previous works [12, 17, 52] report matrix damage that accumulates at the hole and propagates in loading direction. As the material, the boundary conditions, and the expected crack pattern are symmetric regarding the horizontal plane, only half of the specimen is modeled with symmetric boundary conditions to save computation time. For this purpose, the domain is discretized by 12907 quadrilateral 4-node plane stress elements per ply. The symmetry plane used in this case is shown in figure 28. There, the displacement is restricted in the vertical direction. The vertical symmetry is not exploited in this case because potential fiber damage would have to form along this symmetry boundary. The length scales were set to $\ell_f = 2$ mm and $\ell_m = 1$ mm for fiber and

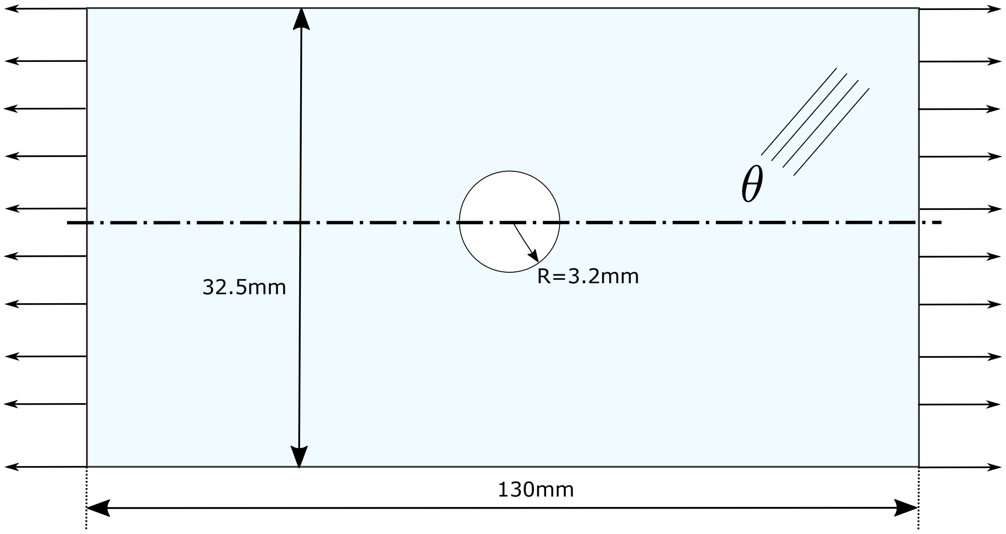

Figure 28: Dimensions and boundary conditions for the laminated open hole tension test. The indicated symmetry plane (dash-dotted line) is used only for the $[0^\circ_4/90^\circ_4]_s$ layup.

Models	Peak load (kN)
Experimental result [12]	25.2
Flatscher [12]	38.4
Broger [52]	39.2
Current implementation	24.3

Table 15: Comparison of the peak loads determined by the current implementation, the implementations in [12, 52] and the experimental result [12].

matrix failure, respectively. The driving forces were set to $\zeta_f = 30$ for fiber damage and $\zeta_m = 0.01$ for matrix damage.
The current implementation shows similar matrix damage patterns as in previous works. Each of them compared their numerical results with the same experiment reported in [12]. The load at failure reported in the experiment is 25.2 kN. All of the numerical results overestimate this peak load. The current implementation can be calibrated to match experiments by tuning the phase-field driving forces. This leads to the peak load being much closer to experimental results than the previous models. All mentioned peak loads are reported in table 15.

The corresponding force-displacement curve with indications of Puck initiation as well as the first time the fiber or matrix damage variable reaches one can be seen in figure 29. In general, the force displacement behavior is linear at first. A

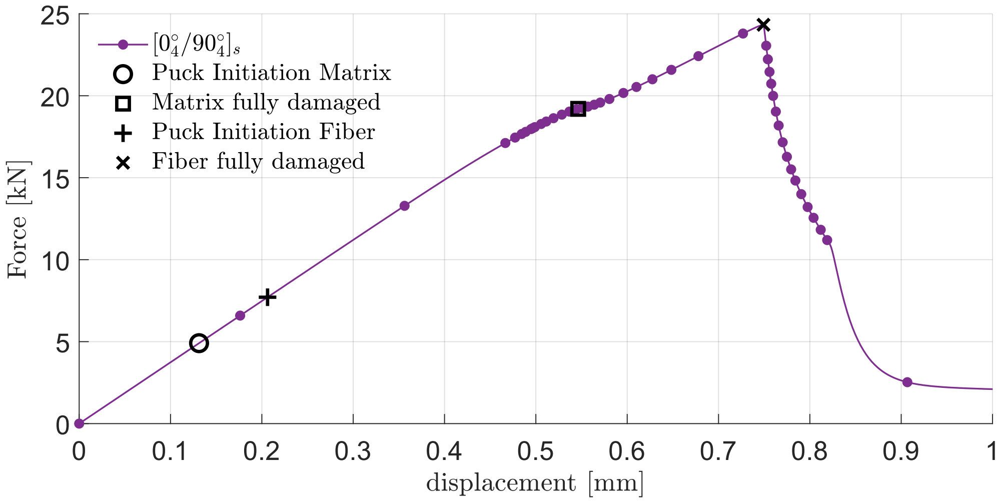

Figure 29: Force displacement curve for an open-hole tension test with a $[0^\circ_4/90^\circ_4]_s$ layup sequence. Indications of Puck initiation for both fiber and matrix as well as the points at which the phase field values for fiber and matrix reach 1 for the first time are given therein.

small drop in reaction force is observed once the accumulating matrix damage approaches one. Afterwards the behavior is linear again until fiber damage accumulates to a greater extent. Fiber damage perpendicular to the loading direction then leads to complete failure of the structure resulting in a sharp drop in force. The resulting damage pattern is compared to the numerical results reported in [17, 51] in figure 30. In addition to the comparison, damage patterns corresponding to higher loading stages are shown in figure 31. Here, matrix damage is shown on the right side while fiber damage values are shown on the left side. It should be noted that the fiber damage plot in figure 31 a) has not yet reached a value of 1. The maximum of the fiber phase field variable is 0.4.
It is observable that a matrix crack forms in loading direction. Once fiber damage accumulates perpendicular to the loading direction, the matrix crack stops growing in the loading direction. Interestingly, matrix damage grows perpendicular to the loading direction with about the same width it formed with in the first place. The first time fiber phase-field extends to the upper boundary occurs at about 0.8214 mm of displacement at the right boundary. In general, the current implementation proves to match experiments well with the chosen driving forces.

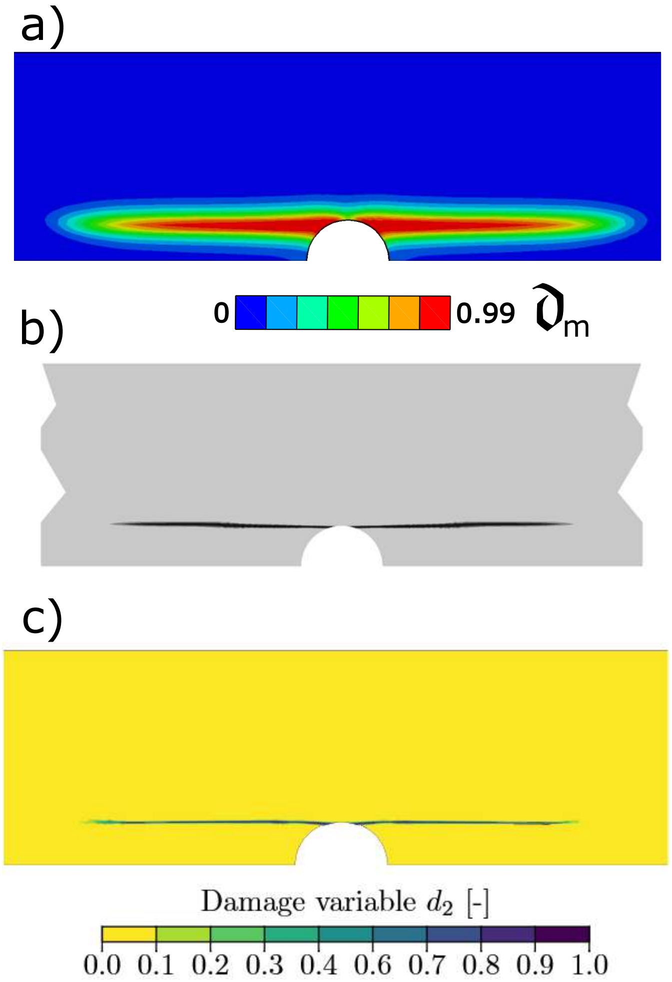

Figure 30: Resulting damage pattern of a) the current implementation at 18.94 kN, b) the model proposed in [51] at an unspecified load level, and c) the model proposed in [17] at 30.36 kN.

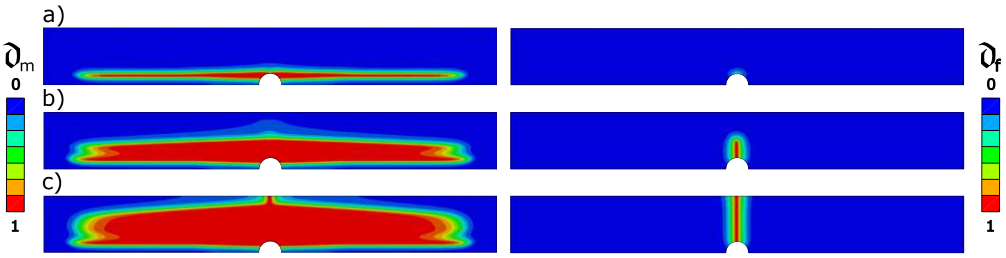

Figure 31: Matrix (left) and fiber (right) phase field for a displacement of the right boundary of a) 0.7056 mm, b) 0.7670 mm which is already past the load peak, and c) 1 mm.

4.3.1 $[45^\circ_4/-45^\circ_4]_s$

For this case no fibers are oriented in loading direction. Due to the fact that crack shielding is prominent in this case [17], the expected crack pattern is not symmetric with respect to the horizontal plane. Therefore, the whole specimen is modeled using 56068 quadrilateral 4-node plane stress elements per ply with refinement around the open hole. The dimensions and boundary conditions are the same as in figure 28 without utilization of the indicated symmetry. The finer discretization is due to the aforementioned need for smaller length scales required to represent the delicate damage patterns accurately. For this purpose, the length scales had to be set to $\ell_f = 0.2$ mm and $\ell_m = 0.1$ mm. The corresponding driving forces were set to $\zeta_f = 1$ and $\zeta_m = 0.005$. The fiber damage driving force is irrelevant, compared to the other layup sequence, as almost no fiber damage is observed in this case [12, 17, 52]. It is important to note that the matrix driving force for the $[45^\circ_4/-45^\circ_4]_s$ case was used as a reference for the order of magnitude for the matrix driving force of the cross-ply layup sequence, which immediately yielded good results when compared to previous works.

In previous works, matrix damage accumulates in both the 45° and −45° plies in a small x-shaped pattern. One of the branches starts to progress while the other does not due to crack shielding which is also apparent in other numerical results [17].

Figure 32 shows the different stages of damage accumulation demonstrated by the current implementation with comparisons to the results of [17, 51]. Regarding the crack propagation, both crack patterns shown in figure 32 b) have the same probability to show up in the current implementation. Numerical inaccuracies then determine which of these two patterns is produced, explaining the difference between the result of [17] and the present result.

The current two-dimensional approach already shows crack patterns similar

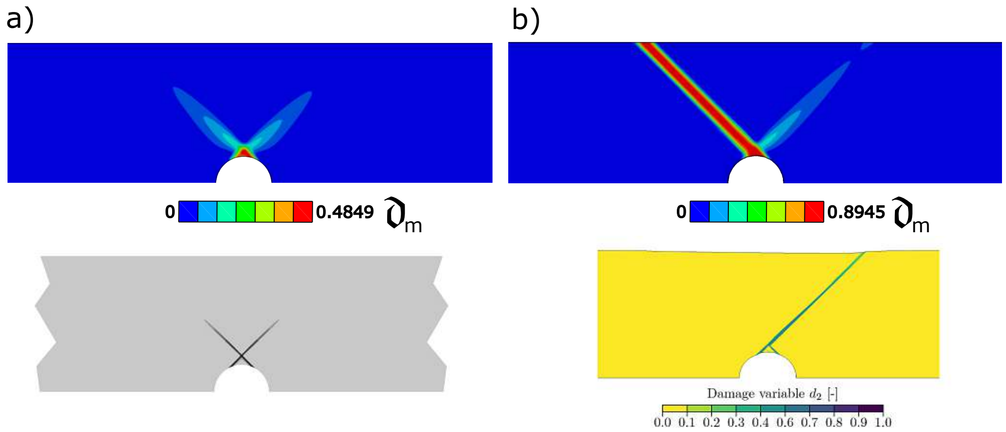

Figure 32: Comparison of a) initial damage to the result in [51] and b) the complete crack pattern to the result in [17].

Models	Peak load (kN)
Experimental result [12]	14.1
Flatscher [12]	10.7
Broger [52]	9.0
Current implementation	11.8

Table 16: Comparison of the peak loads determined by the current implementation, the implementations in [12, 52] and the experimental result [12].

to previous works that used three-dimensional methods. The force-displacement behavior is linear until the structure is fully broken. Previous experiments and numerical results talk about pronounced non-linearity due to plasticity. As plasticity is not taken into account in this model, the non-linearity are not reflected in this example . This behavior along with the point at which Puck activates are shown in figure 33. After reaching the maximum load of 11.84 kN observed in the numerical prediction, the sudden drop in reaction forces indicates unstable crack propagation leading to complete failure. The peak loads observed in previous works as well as the experiment are shown in table 16 and compared to the present result.

4.4 Compact Tension

Li et al. [2] investigated the effect of layup sequences on the fracture behavior of laminated composites. The two types of layups were the blocked ply and dispersed ply sequences. While both types of layup sequences consisted of the same number and type of plies in each corresponding case. For the dispersed plies, each ply had

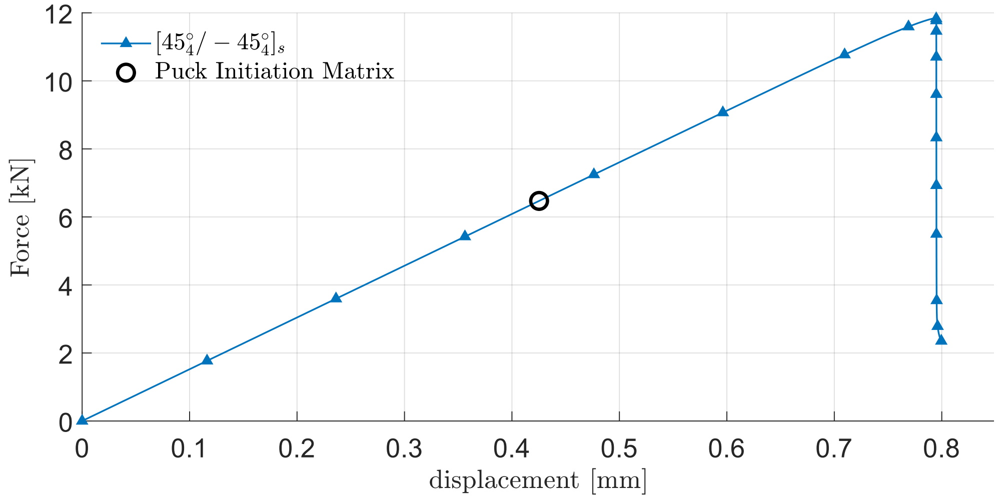

Figure 33: Comparison of a) initial damage to the result in [51] and b) the complete crack pattern to the result in [17].

a different fiber orientation to the next ply, while the blocked ply layup sequences introduced thicker sheets of one fiber orientation by stacking more plies with the same fiber orientation above each other. This leads to a stark contrast in their fracture behavior. While the dispersed ply specimens showed clear fiber failure and only moderate matrix damage, with fiber failure occuring in multiple unstable events. However, the blocked ply specimens were more prone to delamination and matrix damage leading to much more non-linearity in their load-displacement behavior. Furthermore, the quasi-isotropic specimens exhibit much more complex fracture behavior than the cross-ply samples. This behavior cannot be adequately captured with the mesh overlay method. Therefore, only blocked cross-ply results are compared to the current implementation.

The boundary conditions as well as the dimensions of the domain are shown in figure 34 a). In order to mimic the experiments as close as possible, the displacement is applied such that the hole can rotate around a central node without deforming. The whole domain is discretized by 10620 quadrilateral 4-node plane stress elements per ply.

Quantitatively, the force versus pin opening displacement (POD) curve is compared to the measured results [2] in figures 34 b) for the $[0^\circ_2/90^\circ_2]_{2s}$ and c) for the $[0^\circ_4/90^\circ_4]_{2s}$ layups. In both these figures, the same numerical is presented, but for the $[0^\circ_4/90^\circ_4]_{2s}$ case, the reaction forces were scaled accordingly to incorporate the increased thickness. Additionally, figures 34 show the points in the load displacement curves, where the pictures in 36 were taken to facilitate a better qualitative

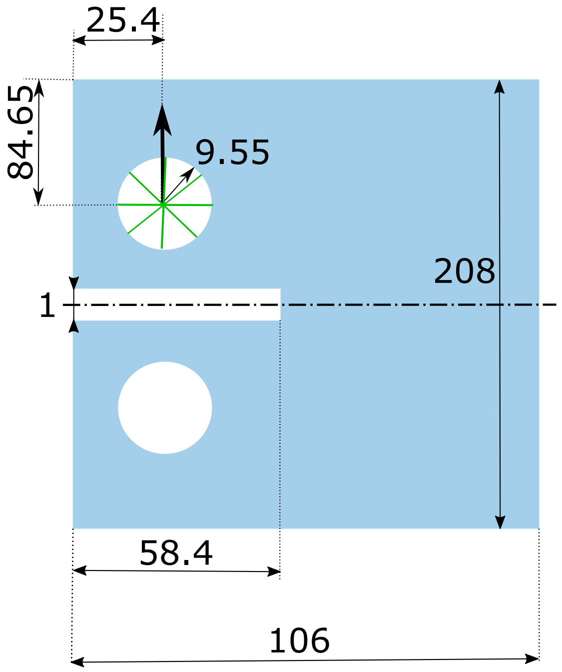

Figure 34: Dimensions and boundary conditions for the laminated compact tension tests. The symmetry plane (dash-dotted line) is used for this simulation. The green lines indicate a rigid connection of the surface to the central node which experiences the displacement. All lengths are considered to be in mm.

comparison. The numerical result is always marked with purple roman numerals, while the experimental results are marked with red and black roman numerals. The Puck matrix damage initiation for this simulation happens at about 0.273 mm of pin opening displacement.

Figures 34 b) and c) generally display a good prediction of the force displacement behavior of the experiment, especially at low loading stages, since, both the experiment and the numerical result show a linear relation between force and displacement with very similar slopes in both cases. Afterwards, the numerical result consistently overpredicts the reaction forces and shows a much longer loading period, where the curve remains linear. This discrepancy is due to the heavy delamination between the plies that occurs in the experiments, which cannot be predicted by the present method. This effect worsens for the $[0^\circ_4/90^\circ_4]_{2s}$ case since the experiments showed even more delamination and other effects with thicker blocked plies. In spite of that, the present implementation generally provides a good match to the experimental results.

The indications in figures 34 b) and c) serve highlights the loading stages at which

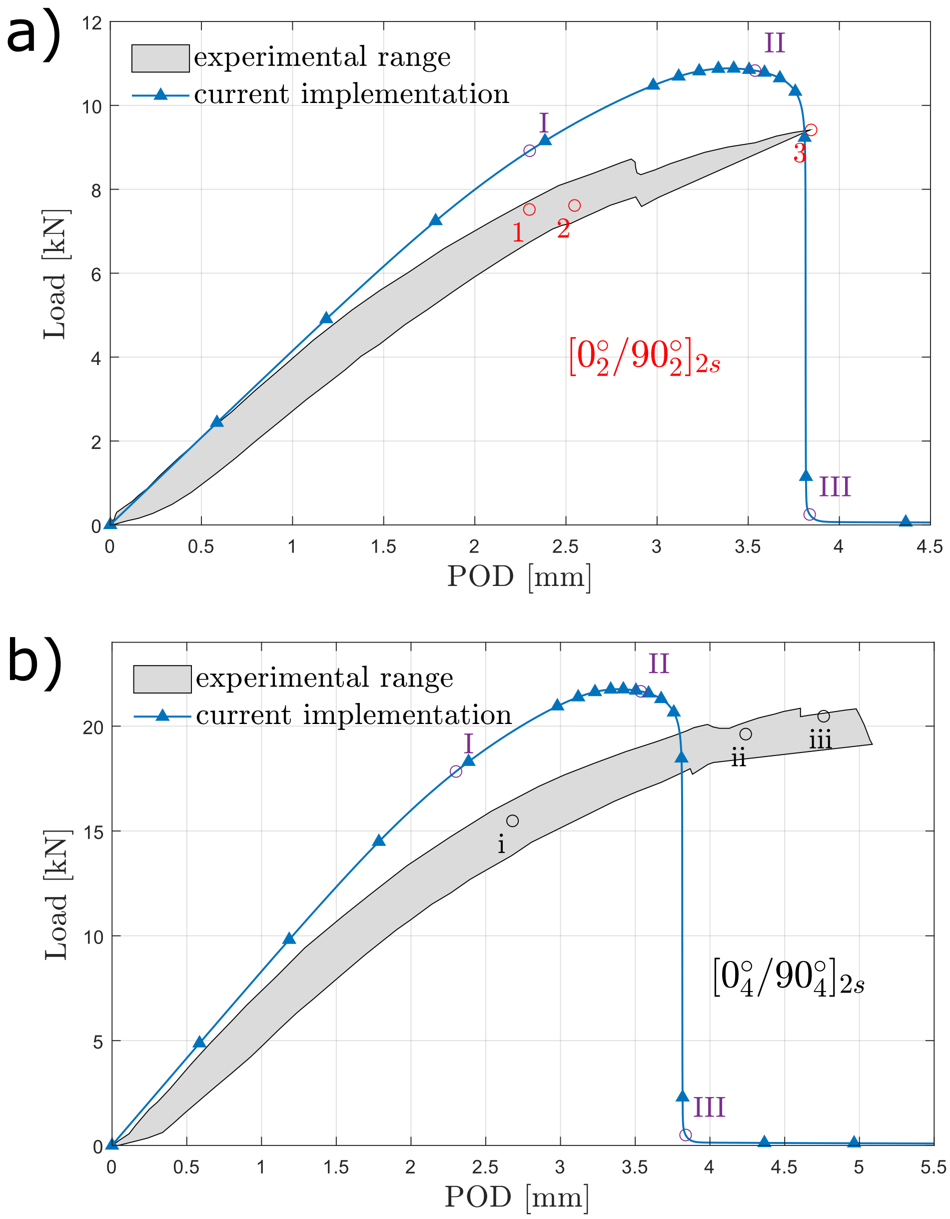

Figure 35: a) Force pin opening displacement (POD) curves corresponding to the $[0^\circ_2/90^\circ_2]_{2s}$ case and b) force pin opening displacement curves corresponding to the $[0^\circ_2/90^\circ_2]_{2s}$ case. The markings with numerals indicate the positions at which the images in figure 36 were taken.

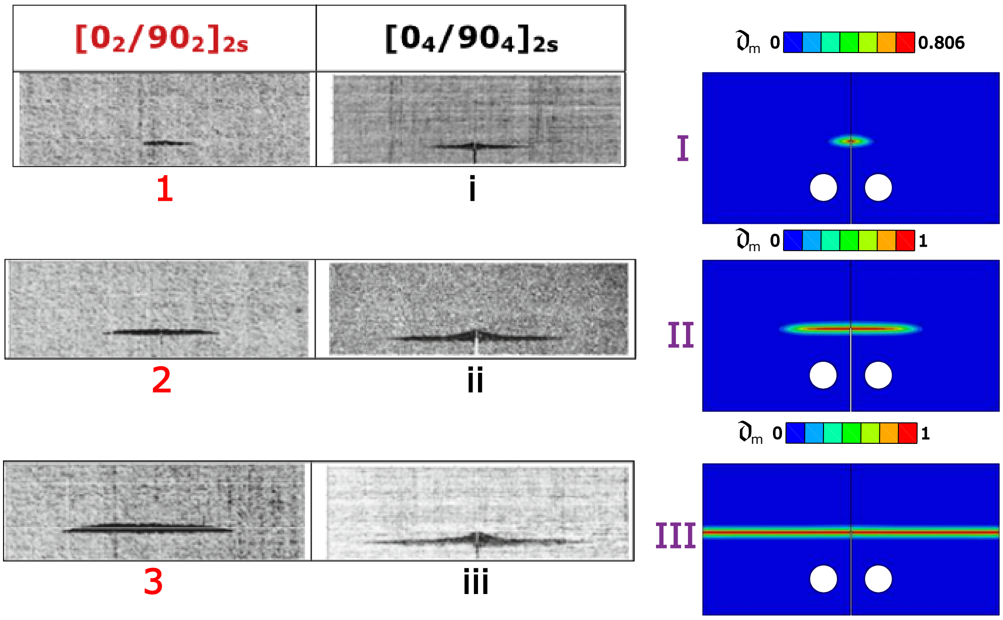

Figure 36: Comparison of the crack propagation of the numerical results (purple roman numerals) to the experimental results (red arabic and small black roman numerals).

the pictures in figure 36 were taken. The initial images 1, i, and I were taken at roughly the same displacement stage, while the second set of pictures differs to a greater extent. This is due to a seemingly unstable crack propagation event that happens in the experiment of the $[0^\circ_2/90^\circ_2]_{2s}$ case between pictures 1 and 2, leading to a larger crack compared to the numerical result at the same displacement. Therefore, picture II was taken at a latter loading stage closer to point ii. The last picture of the numerical result already shows complete failure, while the experiments don't reach complete failure as is the case for the $[0^\circ_2/90^\circ_2]_{2s}$ specimens or failure happens later as for the $[0^\circ_4/90^\circ_4]_{2s}$ samples. The latter fails by the pullout of the 0°-blocks instead of matrix cracking. This may explain the discrepancy in the last row of images in figure 36. The energy needed to further grow the matrix crack is dissipated by delamination and 0°-block pullout, leading to shorter matrix cracks compared to the numerical result. Again, the numerical result provide a reasonably good approximation of the cracks observed in the experiments, even though many of the mechanisms in the experiments are not captured by the current model.

5 Conclusions

The present thesis proposes a multi-phase field model that splits damage in fiber reinforced composites into fiber dominated and matrix dominated failure and approximates them as two separate phase fields. Taking advantage of Puck's failure theory ensures that damage is initiated in a meaningful way. The phase field method then progresses the damage. Furthermore, the presented model is tested for single-ply test cases to show the basic capabilities of the implementations.

5.1 Conclusions single ply model

Seven different test cases are shown for the single ply model. Namely, these are single edge notched tension, open-hole tension, compact tension, centre notched tension, three-point bending, bimaterial system and tension of unnotched specimens. In general, the resulting crack patterns shown by the present implementation are a qualitative match to experimental results. In the case of open hole tension it is shown to be also a qualitative match. Additionally, the simultaneous progression of matrix and fiber damage is shown for cases where the fiber is oriented in loading direction. Fiber reinforced composites are almost always used in some sort of laminate. Therefore, the single-ply results, while insightful, remain mostly theoretical and serve as a kind of plausibility check for the present implementation.

5.2 Conclusion laminated composite model

The proposed model is also used with the mesh overlay method to represent laminated composites. With this method, the implementation for the single ply calculations can be used without modifications to simulate laminated composites, but with some restrictions. Despite these restrictions, the current implementation provided satisfactory results for three different results taken from literature regarding both the emerging crack patterns as well as the reaction forces.

More specifically, the model predicted the load limits of various different coupon tests well compared to previous numerical work. When compared to the open-hole tension results the current implementation provides a good match to previous numerical results in comparing the emerging crack patterns. A quantitative match is achieved when compared to the experimental results. Lastly, the current implementation managed to remain close to the experimental results of compact tension tests., despite the experiments showing highly nonlinear delamination events that cannot be captured by the mesh overlay method. However, both the crack progression and the reaction forces were found to be in good agreement.

6 Outlook

With this groundwork, several different aspects can be investigated. For example, the size effects of fiber-reinforced composites could be investigated in a single ply and a laminate setting. This can be done by simply simulating the same experiment with different dimensions. The same can be said about shape effects on the structural integrity of fiber-reinforced composites by for example varying the notch or hole sizes. Since the present model is only able to handle quasistatic load cases, the incorporation of fatigue effects may be of interest for future developments, in order to predict the fracture behavior for cyclic loading scenarios. Also, an investigation of the length scales in the mesh overlay method could be interesting. The length scales that produced satisfactory results in a single ply setting were much too high to produce similarly satisfactory results when the mesh overlay method was used. Lastly, to accurately predict damage in laminated composites, a three-dimensional approach would lead to the ability to incorporate interply delamination to the model which in turn would lead to more accurate predictions as well. Lastly, an investigation of the calibration of the driving forces could prove valuable, because it leads to the right driving force being known before the simulation.

References

[1] A. Dean et al. A multi phase-field fracture model for long fiber reinforced composites based on the Puck theory of failure. In: *Composite Structures* 251 (2020), p. 112446. ISSN: 0263-8223. DOI: `10.1016/j.compstruct.2020.112446`.

[2] X. Li et al. Experimental study of damage propagation in Over-height Compact Tension tests. In: *Composites Part A: Applied Science and Manufacturing* 40.12 (2009). Special Issue: CompTest 2008, pp. 1891–1899. ISSN: 1359-835X. DOI: `10.1016/j.compositesa.2009.08.017`.

[3] L. Cahill et al. An experimental/numerical investigation into the main driving force for crack propagation in uni-directional fibre-reinforced composite laminae. In: *Composite Structures* 107 (2014), pp. 119–130. ISSN: 0263-8223. DOI: `10.1016/j.compstruct.2013.05.039`.

[4] J. G. Ratcliffe, M. W. Czabaj and T. K. Obrien. ‘Characterizing delamination migration in carbon/epoxy tape laminates’. In: *2012 American Society for Composites 27th Technical Conference 15 US-Japan Conference on Composite Materials*. NF1676L-15085. 2012.

[5] J. G. Ratcliffe and N. V. DeCarvalho. *Investigating delamination migration in composite tape laminates*. Tech. rep. 2014.

[6] A. Ortega et al. Characterization of the translaminar fracture Cohesive Law. In: *Composites Part A: Applied Science and Manufacturing* 91 (2016). CompTest 2015, pp. 501–509. ISSN: 1359-835X. DOI: `10.1016/j.compositesa.2016.01.019`.

[7] A. Turon et al. A damage model for the simulation of delamination in advanced composites under variable-mode loading. In: *Mechanics of Materials* 38.11 (2006), pp. 1072–1089. ISSN: 0167-6636. DOI: `10.1016/j.mechmat.2005.10.003`.

[8] J. Reinoso, M. Paggi and A. Blázquez. A nonlinear finite thickness cohesive interface element for modeling delamination in fibre-reinforced composite laminates. In: *Composites Part B: Engineering* 109 (2017), pp. 116–128. ISSN: 1359-8368. DOI: `10.1016/j.compositesb.2016.10.042`.

[9] P. Maimí et al. A continuum damage model for composite laminates: Part II – Computational implementation and validation. In: *Mechanics of Materials* 39.10 (2007), pp. 909–919. ISSN: 0167-6636. DOI: `10.1016/j.mechmat.2007.03.006`.

[10] A. Quintanas-Corominas et al. A 3D transversally isotropic constitutive model for advanced composites implemented in a high performance computing code. In: *European Journal of Mechanics - A/Solids* 71 (2018), pp. 278–291. ISSN: 0997-7538. DOI: `10.1016/j.euromechsol.2018.03.021`.

[11] P. Camanho, P. Maimí and C. Dávila. Prediction of size effects in notched laminates using continuum damage mechanics. In: *Composites Science and Technology* 67.13 (2007), pp. 2715–2727. ISSN: 0266-3538. DOI: `10.1016/j.compscitech.2007.02.005`.

[12] T. Flatscher et al. Simulations and experiments of open hole tension tests – Assessment of intra-ply plasticity, damage, and localization. In: *Composites Science and Technology* 72.10 (2012), pp. 1090–1095. ISSN: 0266-3538. DOI: `10.1016/j.compscitech.2011.07.021`.

[13] T. Flatscher and H. Pettermann. A constitutive model for fiber-reinforced polymer plies accounting for plasticity and brittle damage including softening – Implementation for implicit FEM. In: *Composite Structures* 93.9 (2011), pp. 2241–2249. ISSN: 0263-8223. DOI: `10.1016/j.compstruct.2011.03.012`.

[14] T. Flatscher, C. Schuecker and H. Pettermann. A constitutive ply model for stiffness degradation and plastic strain accumulation: Its application to the Third World Wide Failure Exercise (Part A). In: *Journal of Composite Materials* 47.20-21 (2013), pp. 2575–2593. DOI: `10.1177/0021998313484075`.

[15] C. Schuecker and H. E. Pettermann. 'Combining Elastic Brittle Damage with Plasticity to Model the Non-linear behavior of Fiber Reinforced Laminates'. In: *Mechanical Response of Composites*. Dordrecht: Springer Netherlands, 2008, pp. 99–117. ISBN: 978-1-4020-8584-0.

[16] C. Schuecker and H. E. Pettermann. Fiber Reinforced Laminates: Progressive Damage Modeling Based on Failure Mechanisms. In: *Archives of Computational Methods in Engineering* 15 (2008), pp. 163–184. DOI: `10.1007/s11831-008-9016-z`.

[17] J. Kaul and H. Pettermann. A constitutive model for fiber reinforced polymer plies – Implicit anisotropic evolution of damage and plasticity based on effective strengths. In: *Composites Part C: Open Access* 4 (2021), p. 100097. ISSN: 2666-6820. DOI: `10.1016/j.jcomc.2020.100097`.

[18] G. Francfort and J.-J. Marigo. Revisiting brittle fracture as an energy minimization problem. In: *Journal of the Mechanics and Physics of Solids* 46.8 (1998), pp. 1319–1342. ISSN: 0022-5096. DOI: `10.1016/S0022-5096(98)00034-9`.

[19] B. Bourdin, G. Francfort and J.-J. Marigo. Numerical experiments in revisited brittle fracture. In: *Journal of the Mechanics and Physics of Solids* 48.4 (2000), pp. 797–826. ISSN: 0022-5096. DOI: `10.1016/S0022-5096(99)00028-9`.

[20] A. A. Griffith. The Phenomena of Rupture and Flow in Solids. In: *Philosophical Transactions of the Royal Society of London. Series A, Containing Papers of a Mathematical or Physical Character* 221 (1921), pp. 163–198. ISSN: 02643952. URL: `http://www.jstor.org/stable/91192`.

[21] E. Tanné et al. Crack nucleation in variational phase-field models of brittle fracture. In: *Journal of the Mechanics and Physics of Solids* 110 (2018), pp. 80–99. ISSN: 0022-5096. DOI: `10.1016/j.jmps.2017.09.006`.

[22] C. Miehe et al. Phase field modeling of fracture in multi-physics problems. Part II. Coupled brittle-to-ductile failure criteria and crack propagation in thermo-elastic–plastic solids. In: *Computer Methods in Applied Mechanics and Engineering* 294 (2015), pp. 486–522. ISSN: 0045-7825. DOI: `10.1016/j.cma.2014.11.017`.

[23] Y.-S. Lo et al. A phase-field model for fatigue crack growth. In: *Journal of the Mechanics and Physics of Solids* 132 (2019), p. 103684. ISSN: 0022-5096. DOI: `10.1016/j.jmps.2019.103684`.

[24] P. Asur Vijaya Kumar et al. Phase field modeling of fracture in Functionally Graded Materials: Γ-convergence and mechanical insight on the effect of grading. In: *Thin-Walled Structures* 159 (2021), p. 107234. ISSN: 0263-8231. DOI: `10.1016/j.tws.2020.107234`.

[25] J. Reinoso et al. Strength prediction of notched thin ply laminates using finite fracture mechanics and the phase field approach. In: *Composites Science and Technology* 150 (2017), pp. 205–216. ISSN: 0266-3538. DOI: `10.1016/j.compscitech.2017.07.020`.

[26] J. Bleyer and R. Alessi. Phase-field modeling of anisotropic brittle fracture including several damage mechanisms. In: *Computer Methods in Applied Mechanics and Engineering* 336 (2018), pp. 213–236. ISSN: 0045-7825. DOI: `10.1016/j.cma.2018.03.012`.

[27] S. Mrunmayee et al. Phase field approach to predict mixed-mode delamination and delamination migration in composites. In: *Composite Structures* 337 (2024), p. 118074. ISSN: 0263-8223. DOI: `10.1016/j.compstruct.2024.118074`.

[28] P. Asur Vijaya Kumar et al. A multi phase-field-cohesive zone model for laminated composites: Application to delamination migration. In: *Composite Structures* 276 (2021), p. 114471. ISSN: 0263-8223. DOI: `10.1016/j.compstruct.2021.114471`.

[29] A. Puck and H. Schürmann. Failure analysis of FRP laminates by means of physically based phenomenological models. In: *Composites Science and Technology* 62.12 (2002), pp. 1633–1662. ISSN: 0266-3538. DOI: `10.1016/S0266-3538(01)00208-1`.

[30] P. Zhang et al. Phase field modeling of fracture in fiber reinforced composite laminate. In: *International Journal of Mechanical Sciences* 161-162 (2019), p. 105008. ISSN: 0020-7403. DOI: `10.1016/j.ijmecsci.2019.07.007`.

[31] I. Jain et al. Adaptive phase-field modeling of fracture in orthotropic composites. In: *Engineering Fracture Mechanics* 292 (2023), p. 109673. ISSN: 0013-7944. DOI: `10.1016/j.engfracmech.2023.109673`.

[32] D. Pranavi, A. Rajagopal and J. Reddy. Interaction of anisotropic crack phase field with interface cohesive zone model for fiber reinforced composites. In: *Composite Structures* 270 (2021), p. 114038. ISSN: 0263-8223. DOI: `10.1016/j.compstruct.2021.114038`.

[33] Hirshikesh, E. Martínez-Pañeda and S. Natarajan. Adaptive phase field modelling of crack propagation in orthotropic functionally graded materials. In: *Defence Technology* 17.1 (2021), pp. 185–195. ISSN: 2214-9147. DOI: `10.1016/j.dt.2020.03.004`.

[34] C. Miehe, M. Hofacker and F. Welschinger. A phase field model for rate-independent crack propagation: Robust algorithmic implementation based on operator splits. In: *Computer Methods in Applied Mechanics and Engineering* 199.45 (2010), pp. 2765–2778. ISSN: 0045-7825. DOI: `10.1016/j.cma.2010.04.011`.

[35] K. Pham et al. Gradient Damage Models and Their Use to Approximate Brittle Fracture. In: *International Journal of Damage Mechanics* 20.4 (2011), pp. 618–652. DOI: `10.1177/1056789510386852`.

[36] J.-Y. Wu. A unified phase-field theory for the mechanics of damage and quasi-brittle failure. In: *Journal of the Mechanics and Physics of Solids* 103 (2017), pp. 72–99. ISSN: 0022-5096. DOI: `10.1016/j.jmps.2017.03.015`.

[37] Z. Pan, L.-W. Zhang and K. Liew. Adaptive surrogate-based harmony search algorithm for design optimization of variable stiffness composite materials. In: *Computer Methods in Applied Mechanics and Engineering* 379 (2021), p. 113754. ISSN: 0045-7825. DOI: `https://doi.org/10.1016/j.cma.2021.113754`.

[38] P. Prabhakar and A. M. Waas. A novel continuum-decohesive finite element for modeling in-plane fracture in fiber reinforced composites. In: *Composites Science and Technology* 83 (2013), pp. 1–10. ISSN: 0266-3538. DOI: `10.1016/j.compscitech.2013.03.022`.

[39] A. Kumar and T. Sain. Phase field-based cohesive zone approach to model delamination in fiber-reinforced polymer composites. In: *Composite Structures* 329 (2024), p. 117751. ISSN: 0263-8223. DOI: `10.1016/j.compstruct.2023.117751`.

[40] S. Hallett et al. An experimental and numerical investigation into the damage mechanisms in notched composites. In: *Composites Part A: Applied Science and Manufacturing* 40.5 (2009), pp. 613–624. ISSN: 1359-835X. DOI: `10.1016/j.compositesa.2009.02.021`.

[41] J. Felger, N. Stein and W. Becker. Mixed-mode fracture in open-hole composite plates of finite-width: An asymptotic coupled stress and energy approach. In: *International Journal of Solids and Structures* 122-123 (2017), pp. 14–24. ISSN: 0020-7683. DOI: `10.1016/j.ijsolstr.2017.05.039`. URL: `https://www.sciencedirect.com/science/article/pii/S0020768317302524`.

[42] S. Jose et al. Intralaminar fracture toughness of a cross-ply laminate and its constituent sub-laminates. In: *Composites Science and Technology* 61.8 (2001), pp. 1115–1122. ISSN: 0266-3538. DOI: `10.1016/S0266-3538(01)00011-2`. URL: `https://www.sciencedirect.com/science/article/pii/S0266353801000112`.

[43] A. Kumar and T. Sain. A 3D multi-phase-field model for orientation-dependent complex crack interaction in fiber-reinforced composite laminates. In: *Engineering Fracture Mechanics* 303 (2024), p. 110097. ISSN: 0013-7944. DOI: `10.1016/j.engfracmech.2024.110097`.

[44] S. D. Nonn. *Effects of defects and damage localization in carbon fiber reinforced polymer lightweight structures*. eng. 2018. URL: `https://resolver.obvsg.at/urn:nbn:at:at-ubl:1-24676`.

[45] R. Adams and P. Cawley. A review of defect types and nondestructive testing techniques for composites and bonded joints. In: *NDT International* 21.4 (1988), pp. 208–222. ISSN: 0308-9126. DOI: `https://doi.org/10.1016/0308-9126(88)90333-1`. URL: `https://www.sciencedirect.com/science/article/pii/0308912688903331`.

[46] S. Hörrmann, A. Adumitroaie and M. Schagerl. Through-thickness fatigue behavior of non-crimp fabrics featuring manufacturing defects. In: *Procedia Structural Integrity* 2 (2016). 21st European Conference on Fracture, ECF21, 20-24 June 2016, Catania, Italy, pp. 158–165. ISSN: 2452-3216. DOI: `https:`

//doi.org/10.1016/j.prostr.2016.06.021. URL: https://www.sciencedirect.com/science/article/pii/S245232161630021X.

[47] S. Hörrmann, A. Adumitroaie and M. Schagerl. The effect of ply folds as manufacturing defect on the fatigue life of CFRP materials. In: *Fracture and Structural Integrity* 10.38 (2024/11/21 2016), Pages 76–81. DOI: 10.3221/IGF-ESIS.38.10. URL: https://www.fracturae.com/index.php/fis/article/view/1772.

[48] S. Hörrmann et al. The effect of fiber waviness on the fatigue life of CFRP materials. In: *International Journal of Fatigue* 90 (2016), pp. 139–147. ISSN: 0142-1123. DOI: https://doi.org/10.1016/j.ijfatigue.2016.04.029. URL: https://www.sciencedirect.com/science/article/pii/S0142112316300834.

[49] S. Nonn, C. Kralovec and M. Schagerl. Damage mechanisms under static and fatigue loading at locally compacted regions in a high pressure resin transfer molded carbon fiber non-crimp fabric. In: *Composites Part A: Applied Science and Manufacturing* 115 (2018), pp. 57–65. ISSN: 1359-835X. DOI: 10.1016/j.compositesa.2018.09.011.

[50] S. Nonn et al. Application of electrical impedance tomography to an anisotropic carbon fiber-reinforced polymer composite laminate for damage localization. In: *Composites Science and Technology* 160 (2018), pp. 231–236. ISSN: 0266-3538. DOI: 10.1016/j.compscitech.2018.03.031.

[51] T. Flatscher. 'A constitutive model for the elasto-plasto-damage ply behavior in laminated FRP composites: its development, implementation and application in FEM simulations'. Available at reposiTUm https://resolver.obvsg.at/urn:nbn:at:at-ubtuw:1-31444. [Dissertation. Technische Universität Wien], 2010.

[52] J. Broger. 'Adaptation of an elasto-plasto-damage model from Abaqus/Standard to Abaqus/Explicit and its application to laminated FRP composites'. Available at reposiTUm https://doi.org/10.34726/hss.2014.3960. [Diploma Thesis. Technische Universität Wien], 2014.